DYNAMIC TIDE-TSUNAMI INTERACTION IN THE HUDSON RIVER ESTUARY

BY

MICHAEL SHELBY, STEPHAN T. GRILLI, ANNETTE R. GRILLI

DEPT. OF OCEAN ENG., UNIVERSITY OF RHODE ISLAND

RESEARCH REPORT NO. CACR-15-10
OCTOBER 2015

Supported by the National Tsunami Hazard Mitigation Program
National Weather Service Grant NA14NWS4670041

CENTER FOR APPLIED COASTAL RESEARCH

Department of Civil and Environmental Engineering
University of Delaware
Newark, Delaware 19716, USA

Abstract

This work was performed as part of a tsunami inundation mapping activity carried out along the US East Coast since 2010, under the auspice of the National Tsunami Hazard Mitigation program (NTHMP). In our geographic area, two main estuaries with significant tidal forcing were identified, which are bordered by numerous critical facilities (power plants, major harbors,...) as well as densely built areas located at low level: the Hudson River Estuary and Chesapeake Bay. The present report details work done in the Hudson River Estuary (HRE), with a focus on the Southern Manhattan, Hudson and East River areas. For NTHMP, tsunami inundation maps are developed in terms of envelopes of maximum flooding, by simulating coastal tsunami propagation for selected Maximum Probable Tsunamis (PMT) originated in the Atlantic ocean margin and basin, using a static reference tide level in the tsunami propagation and inundation modeling, equal to Mean High Water (MHW). Here, following a new methodology, we simulate dynamic interactions in the HRE between the incident PMTs and a tide achieving MHW at high tide, and evaluate whether this leads to increased flooding as compared to the static level approach; each PMT is simulated for 4 different phases of the tide in order to identify conditions that maximize tsunami impact.

In our modeling methodology, we first separately simulate the dominant M2 tide and the three most significant incident tsunamis (PMTs) for the HRE, whose sources are located in the Atlantic Ocean Basin or on the continental shelf off of the HRE; this is done using the nonlinear and dispersive long wave model FUNWAVE-TVD, in coarse to fine nested grids. Bottom friction coefficients used in the simulation grids are calibrated for the tide to achieve the local spatially averaged MHW level at high tide, based on observations at NOAA tide gages, in the finer grid encompassing the HRE. The combined tide-tsunami simulations are then performed, for 4 phases of the tides; these correspond to each tsunami arriving at Sandy Hook, NJ's gage: 1.5h ahead, concurrent with, 1.5h after, and 3h after the local high tide. Such combined simulations are forced along the offshore boundary of the medium size grid, by linearly superposing time series of surface elevation and horizontal currents of the calibrated tide and each tsunami wavetrain; this offshore boundary is located on the shelf, in deep enough water for a linear approximation to be accurate, in view of the tide and tsunami elevations. Dynamic tide-tsunami simulations are then performed with FUNWAVE-TVD, using the combined time

series as boundary conditions; note these include both incident and reflected waves and thus satisfy an open boundary condition along the grid boundary. For each considered phase of the tide, both static and dynamic tide-tsunami simulations are repeated for incident tsunamis caused by: (i) the Cumbre Vieja Volcano (CVV) flank Collapse in the Canary Islands (with a 80 km^3 volume representing the most likely extreme scenario); (ii) a M9 coseismic source in the Puerto Rico Trench (PRT); and a large submarine mass failure (SMF) in the Hudson River canyon of parameters similar to the 165 km^3 historical Currituck slide, which is used as a local proxy for the maximum possible SMF. Four levels of nested grids are used, from 1 arc-min in the deep ocean down to a 39 m Cartesian grid in the HRE.

Results show that overall, for most phases of the tide and for the 3 PMTs, the dynamic simulations lead to increased inundation (by up to 0.2 to 0.8 m depending on location) in the HRE as compared to simulations over a static MHW level, with the worst-case scenario, leading to maximum inundation in the HRE, being the CRT SMF proxy tsunami. In all tide phase cases, nonlinear interactions between tide and tsunami currents change the elevation, current, and velocity of propagation of the various waves in the incident wave trains, mostly in the shallower water area of the HRE where bottom friction dominates, as compared to a simple linear superposition of wave elevations and currents. Site specific effects in the complex geometry and bathymetry of the HRE also appear to play an important role in the interactions of tide and tsunamis and on how much increase in inundation this leads to and where.

1 Introduction

Tides and tsunamis are both long waves, whose individual propagation is governed by long wave theories (Dean and Dalrymple, 1991), such as linear Stokes theory in deep water and Saint Venant or Boussinesq equations in shallow water, depending on the relative magnitude of nonlinearity and dispersive effects. In deep water, tsunamis are not affected by tides, because both the tidal range is small with respect to depth and tide-induced currents are very weak. Hence, tsunami phase speed and shoaling are not significantly affected by the small change in water depth caused by tides and the current associated with the tsunami is usually stronger than tidal current. The same applies to shallow coastal water areas with simple bathymetry and fairly

straight coastlines. In such a situation, which is prevalent for most of the ocean-exposed US east coast, from Florida to Massachusetts, while tide-induced currents and range may become larger, with the latter being more significant with respect to local depth, tsunami coastal hazard in terms of maximum inundation and runup, can still be accurately assessed by modeling tsunami propagation with respect to a static reference level corresponding to a large tide (typically the 10% exceedence tide or the mean high water (MHW) level). For instance, this was the approach followed for performing tsunami inundation mapping in Ocean City, MD due to tsunamis caused by submarine mass failures (SMF) along the upper US east coast (Grilli et al., 2015).

When assuming a static increase of the mean water level (MWL) in model simulations, both tsunami phase speed and elevation will be affected by the increased depth, yielding larger inundation further onshore. However, in coastal regions where tidal range is large and/or bathymetry is complex (e.g., creating funneling effects), tide-induced flows may be both large and strongly varying in space. In such cases, tsunami-tide interactions may need to be more carefully and accurately evaluated, in order to achieve a conservative coastal hazard assessment. This requires, in particular, considering whether nonlinear interactions between tide and tsunami flow velocities and elevations may lead to more hazardous conditions than with the standard maximum static level approach. Along the US East Coast, significant tide-tsunami interactions could occur around the mouth of a few large and complex estuaries, that are also usually highly populated areas having numerous critical infrastructures (such as major harbors and powerplants), with prominent examples being New York, NY in the Hudson River estuary and Norfolk, VA near the mouth of the James River estuary in the Chesapeake Bay.

Since 2010, under the auspices of the US National Tsunami Hazard Mitigation Program (NTHMP; http://nthmp.tsunami.gov/index.html), together with colleagues from the University of Delaware, the authors have been involved with the modeling of coastal tsunami hazard and the development of tsunami inundation maps along the US East coast (e.g., Tehranirad et al., 2014) including at these strongly tide-affected estuaries, under the effects of all the Probable Maximum Tsunamis (PMTs) that could occur in the Atlantic Ocean basin. These PMTs included (Fig. 1 and 2; see also ten Brink et al., 2008; ten Brink et al., 2014): (i) near-field submarine mass failures (SMFs) on or near the continental shelf break, represented along the upper east coast

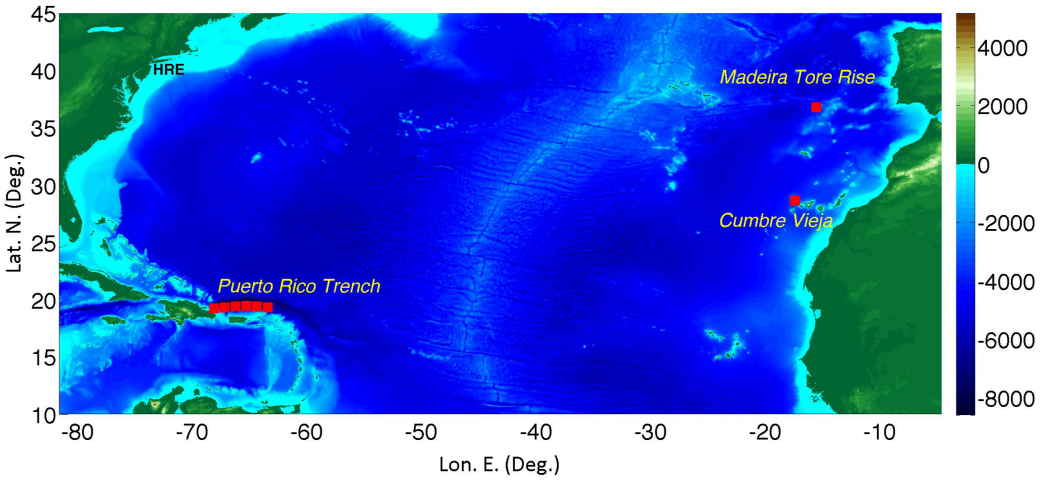

Figure 1: Area of the 1 arc-min Atlantic Ocean basin Grid G4 (Table 1), with marked locations of the three PMT far-field sources used in NTHMP work: LSB, CVV and PRT. The "HRE" label marks the location of the Hudson River Estuary mouth. Color scale is bathymetry (< 0) and topography (> 0) in meters, from ETOPO-1 data.

by four large SMF proxies, modeled at selected locations with the characteristics of the historical 165 km^3 Currituck (CRT) underwater landslide (Grilli et al., 2009, 2015) (details will be provided later; Fig. 2); (ii) an extreme hypothetical M9 seismic event occurring in the Puerto Rico Trench (Grilli et al., 2010, 2013b); (iii) a repeat of the historical 1755 M9 earthquake occurring in the Azores convergence zone (Madera Tore Rise; Barkan et al., 2009; Grilli et al., 2013a); and (iv) an extreme flank collapse (80 km^3 and 450 km^3 scenarios) of the Cumbre Vieja Volcano (CVV) in the Canary Islands (Abadie et al., 2012; Tehranirad et al., 2015). To carry out this tsunami inundation mapping work, a large number of tsunami simulations were performed using the fully nonlinear and dispersive model FUNWAVE-TVD (Shi et al., 2012; Kirby et al., 2013), by one-way coupling in a series of coarse to finer nested grids. According to the standard methodology, in the simulations, the reference level in the coastal grids was statically set to a high tide value (such as the Mean High Water level; MHW level). Hence, potential dynamic interactions between tide- and tsunami-induced flows were neglected.

To date, interactions between tide and tsunami waves have only

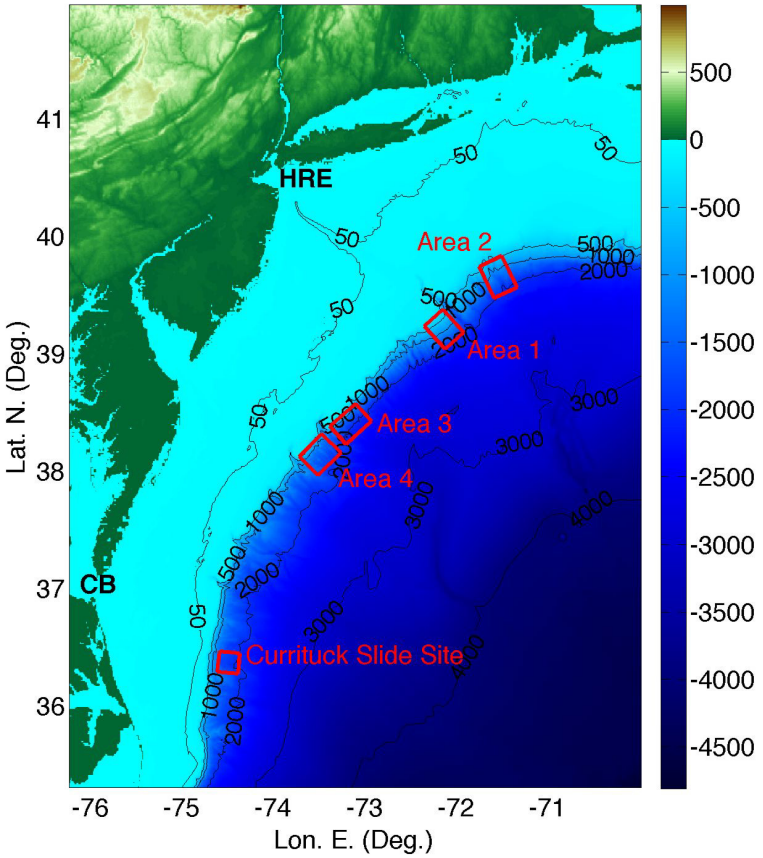

Figure 2: Map of upper US East Coast region encompassing the two large estuaries considered in the NTHMP tide-tsunami interaction work (Chesapeake Bay (CB) and Hudson River Estuary (HRE)), representing the area used for simulating SMF tsunami hazard (from Virginia to Cape Cod). Red boxes mark locations of the historical Currituck slide site and of four Areas (1-4) identified for siting potentially large tsunamigenic SMF sources (Grilli et al., 2009, 2015) and where SMF Currituck proxies were modeled (Grilli et al., 2015). Depth is in meters, in the color scale and bathymetric contours.

rarely been studied. Kowalik et al. (2006) first hypothesized that significant effects due to tsunamitide interactions should be observed in the tidal and tsunami currents. Kowalik and Proshutinsky (2010) first modeled tide-tsunami interactions in a simple channel and then in Cook Inlet (Alaska), which has one of the largest tidal ranges in North America. They found that results significantly differed from a simple linear superposition of separate simulations of tide and tsunami, and that maximum elevations depended on the tide amplitude and phase; with tsunami being intensified or damped, depending on mean basin depth, which is regulated by tides. They concluded that, in their simulations, the main effects of the tide were to change water depth, thus affecting tsunami phase speed, propagation and amplification, and dissipation by bottom friction. These, however, were site specific conclusions and it is thus not possible to a priori predict the effects of tsunamitide interactions without simulating tsunamis together with tidal forcing. Zhang et al. (2011) performed high resolution simulations of the impact of the 1964 Prince William Sound tsunami on the US Pacific Northwest coast, with and without dynamic tide effects. They evaluated the tidal influence on wave elevation, velocity and inundation. Their results showed that the tide, as could be expected, had minimal effects near the open coast, but significantly affected both wave runup and inundation near and in estuaries and rivers. On this basis, they concluded that dynamic tsunamitide interactions should be considered in tsunami studies done near and in estuaries, as these could account for 50% of the observed runup and up to 100% of the inundation in some cases. Yeh et al. (2012) and Tolkova (2013) modeled tsunami-tide interactions in the Columbia River (Oregon), to better understand the observed 100 km upstream propagation of the Tohoku 2011 tsunami in the river. Tolkova found that tsunami waves propagated further on a rising tide in the lower portion of the river; however, upstream the tsunami propagated further at the maximum high tide. The simulations performed also showed potential amplification of tsunami waves directly after high tide. Tolkova concluded that the interaction of the two long waves is completely dependent on the specific environment in which the interaction occurs, which justifies performing site-specific studies. More recently, performing similar studies based on data from a river In Japan, Tolkova et al. (2015) concluded that the Tohoku 2011 tsunami had caused increased surface elevations in the river by hindering drainage. This may translate to increased tsunami surface elevations during a tidal ebb.

The combined effects of tsunami and tide were recently modeled in Chesapeake Bay by Tajali-Bakhsh et al. (2014), as part of tsunami hazard assessment made for a nuclear power plant located upstream of the James River within the Bay. They considered the M2 tidal component in the Bay and combined it for different phases of the two worst case scenario PMTs estimated this area, i.e., tsunamis generated by an extreme CVV flank collapse scenario and the historical Currituck underwater slide, whose site is located near the mouth of the Bay (Geist et al., 2009; Grilli et al., 2015) (Fig. 2).

Here, following a similar methodology, we simulate the combined effects of tidal phase and current magnitude on the evolution of tsunami waves in the Hudson River Estuary (HRE). Based on the earlier work discussed above, regarding incident tsunamis, we select the three largest PMTs used to perform NTHMP inundation mapping in the area, which represent the most likely extreme events that can potentially affect this region of the U.S. east coast. These are caused by: (i) A Currituck SMF proxy sited on the continental slope near the Hudson River (Grilli et al., 2015) (see "Study Area 1" in Fig. 2); (ii) A 80 km^3 flank collapse of the Cumbre Vieja Volcano in the Canary Islands (Abadie et al., 2012; Tehranirad et al., 2015); and (iii) A magnitude 9.0 earthquake in the Puerto Rico Trench (Grilli et al., 2010, 2013b). The HRE/New York Bay tidal system has particularly strong currents (1-2 kts) and has also been identified as one of the highest risk areas along the U.S. east coast for flooding caused by a tsunami resulting from a submarine mass failure (SMF) in the Hudson River Canyon (Grilli et al., 2009); as indicated above, this has led to defining a CRT SMF proxy sources in the HRE canon area (Fig. 2). Besides the importance of performing systematic and conservative tsunami hazard assessment for all the U.S. coastal areas, as part of NTHMP, the HRE provides another interesting system where to assess the importance of nonlinear exchanges of energy between tide and tsunami, similar to the work done by Tolkova (2013) in the Columbia River. There, Tolkova found that tsunami signals propagating with the low tide were lost, while those traveling with the high tide were preserved or amplified. This was most apparent at the farthest upstream station for which data for the Tohoku 2011 tsunami was collected. If the Hudson River results are consistent with these findings, differences between static and dynamic tide-tsunami simulations will be amplified at upstream locations. It should be noted that such phenomena were observed for tsunamis propagating up the James River by Tajali-Bakhsh et al.

Grid/ Type	SW Lat. (N deg.)	NE Lat. (N deg.)	SW Lon. (W deg.)	NE Lon. (W deg.)	Res.	N_x	N_y
G4/S	10	45	82	5	1 min	4,620	2,100
G3a/C	36.396	41.885 N	74.994	69.25	616 m	788	990
G3b/C	39.171	41.904	74.829	71.138	616 m	512	489
G2/C	40.003	41.355	74.437	72.266	154 m	1,188	980
G1/C	39.171	40.900	74.829	73.775	38.5 m	459	1,504

Table 1: Parameters of model grids (Figs. 1 and 3) used in FUNWAVE-TVD to compute the propagation of far-field (G4, G3b, G2, G1) sources (CVV and PRT) and near-field (G3b, G2, G1) tsunami sources (CRT SMF proxy 1; Fig. 2), and tides (G2, G1). "Res." refers to resolution of Spherical (S) or Cartesian (C) type grids and N_x and N_y indicate the number of grid cells in each direction.

(2014).

Here, to assess dynamic tide-tsunami interactions, we perform two sets of simulations. First, for each PMT, we simulate tsunami propagation into the HRE when assuming a static level equal to the local MHW tidal level. Then we perform joint tide-tsunami simulations, for a tidal forcing that achieves a MHW level in the HRE for the maximum tide level. The methodology for performing the latter joint simulations is that first introduced by Tajali-Bakhsh et al. (2014), which is detailed in the next section. We then briefly detail the computational model and grid set-up, and then present and compare results of the two sets of simulations.

2 Modeling methodology and model grids

All the model simulations, both tide and tsunamis, or these jointly, are performed using the fully nonlinear and dispersive Boussinesq model FUNWAVE (Wei et al., 1995; Grilli et al., 2007, 2010; Ioualalen et al., 2007), in its latest Cartesian (Shi et al., 2012) and spherical (Kirby et al., 2013) implementations referred to as FUNWAVE-TVD. FUNWAVE-TVD is fully parallelized for an efficient solution on shared memory clusters and has a more efficient Total Variation Diminishing (TVD) algorithm to follow breaking wave fronts in shallow water. The model has a quadratic bottom friction term controlled by a Manning friction coefficient n and, unlike the original FUNWAVE, it models

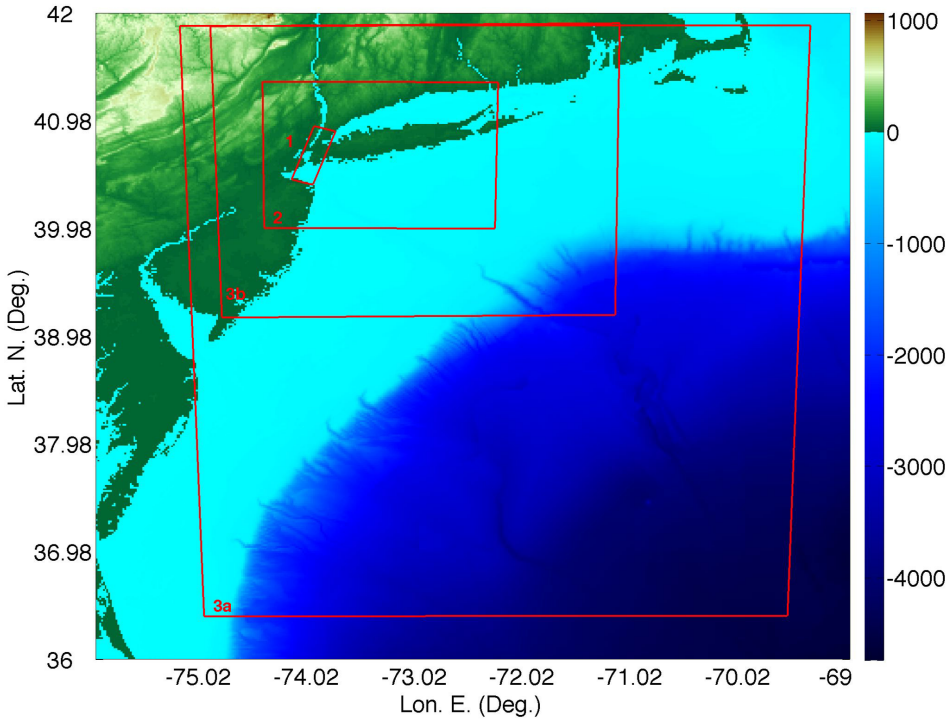

Figure 3: Computational domains used in tide, tsunami and tide-tsunami simulations with FUNWAVE-TVD (labeled red boxes correspond to grids defined in Table 1). Tide only simulations are initiated in Grid 3b, and then nested into Grids 2 and Grid 1. Besides the 1 arc-min Grid G4 (Fig. 1), the far-field (CVV, PRT) tsunami simulations use the nested grids: G3b, G2 and G1, and the near-field CRT proxy SMF tsunami simulations use grids G3a, G2, and G1. All tide-tsunami simulations start in grid G2 and end in grid G1. Color scale is bathymetry (< 0) and topography (> 0) in meters.

dissipation in breaking waves by turning off dispersive terms in areas where breaking is detected based on a breaking index criterion. While FUNWAVE-TVD's Cartesian implementation is fully nonlinear, its spherical implementation is only mildly nonlinear; hence, it is only applicable in areas where tsunami elevation over local depth is perhaps not more than 10 percent. Therefore, in tsunami simulations, spherical grids will be fairly coarse and used to model large ocean areas in relatively deeper waters, whereas Cartesian grids will have a higher resolution and be used to model coastal tsunami impact. This approach was successfully used to model the Tohoku 2011 tsunami (Grilli et al., 2013; Kirby et al., 2013). Both implementations of FUNWAVE-TVD have been fully validated against standard benchmarks, as part of the NTHMP work (Tehranirad et al., 2011; Shi et al., 2012).

Simulations with FUNWAVE-TVD, whether spherical or Cartesian, are performed in several levels of nested grids using a one-way coupling methodology. This works by computing time series of free surface elevations and currents in a coarser grid level, for a large number of numerical gages (stations) defined along the boundary of the finer grid level. Computations in the finer nested grid level are then performed using these time series as boundary conditions. With this approach, reflected waves propagating from inside the area covered by each finer grid are included in the time series computed in the coarser grids along the finer grid boundaries, thus satisfying an open boundary condition. For far-field tsunami simulations, to reduce reflection in the first coarsest grid level (here the 1 arc-min Atlantic Ocean basin grid used to compute the transoceanic propagation of the CVV and PRT sources; Fig. 1), 200 km thick sponge (absorbing) layers are specified along all the open boundaries. For the near-field CRT SMF proxy tsunami, the first level of grid is initialized with the surface elevation and horizontal velocity computed using the three-dimensional model NHWAVE (Ma et al., 2012) (see details in Grilli et al., 2015)

For the dynamic tide-tsunami simulations, we follow the methodology that was first applied by Tajali-Bakhsh et al. (2014) in the Chesapeake Bay estuary, i.e., to:

1. Simulate the propagation of the selected PMTs from their source, in a series of nested grids, to a moderate resolution (here 154 m resolution grid G2; Fig. 3; Table 1) regional grid encompassing the HRE (Fig. 3).

2. Simulate a large tide whose maximum elevation reaches the local MHW level in the HRE area and calibrate results using tide measurements available at a series of NOAA tide gage; adjust bottom friction values in the model if necessary, to achieve a better agreement. The tidal forcing itself (both surface elevation and current) is obtained from a separate global model (detailed later) and specified along the boundary of a regional grid encompassing the site (here the 616 m resolution G3b grid; Fig. 3; Table 1).

3. Then, jointly simulate tide and tsunami, by superimposing incoming tsunami wave elevations and velocities with tidal forcing, along the offshore boundary of a computational grid selected where depth is large enough to justify their linear superposition (here, grid G2).

4. Finally, simulate effects of tide phase on the three incident tsunamis by considering 4 different phases when peak tsunami and time-shifted tide signals are superimposed along the boundary of grid G2.

Besides their footprint, resolution and types, the model grids require a depth matrix that is developed by interpolating bathymetric and topographic data of resolution commensurate with that of the grids. All the model grid parameters are defined in Table 1, and their footprints are shown in Figs. 1 and 3. In our NTHMP work, bathymetry and topography for these grids are interpolated from the most accurate source available, i.e., 1 arc-min ETOPO-1 data in deeper water, 3 arc-sec (90 m) NOAA Coastal Relief model data (NOAA-NGDC, 2013) over the shelf, and 1/3 arc-sec (10 m) NTHMP or Federal Emergency Management Agency (FEMA) Region II Digital Elevation Models (DEMs) wherever available FEMA (2014). However, much of the detailed bathymetry provided by NOAA for coastal hazard assessment has a notable absence of data in the vicinity of Manhattan Island. This region is critical for considering tsunami effects in the Hudson River. Near-shore bathymetry in this region with a resolution of about 8 meters was obtained from FEMA (Fig. 4; FEMA (2014)). Thus, grid G4 depth matrix is based on ETOPO-1 data, while that of grids G3a,b is based on ETOPO-1 and 90 m DEM data. All of grid G1 and part of grid G2's depth matrix is based on FEMA's 8 m DEM and parts of Grid G2 that are not included in this high-resolution data were completed using NOAA's 90 m DEM. Fig-

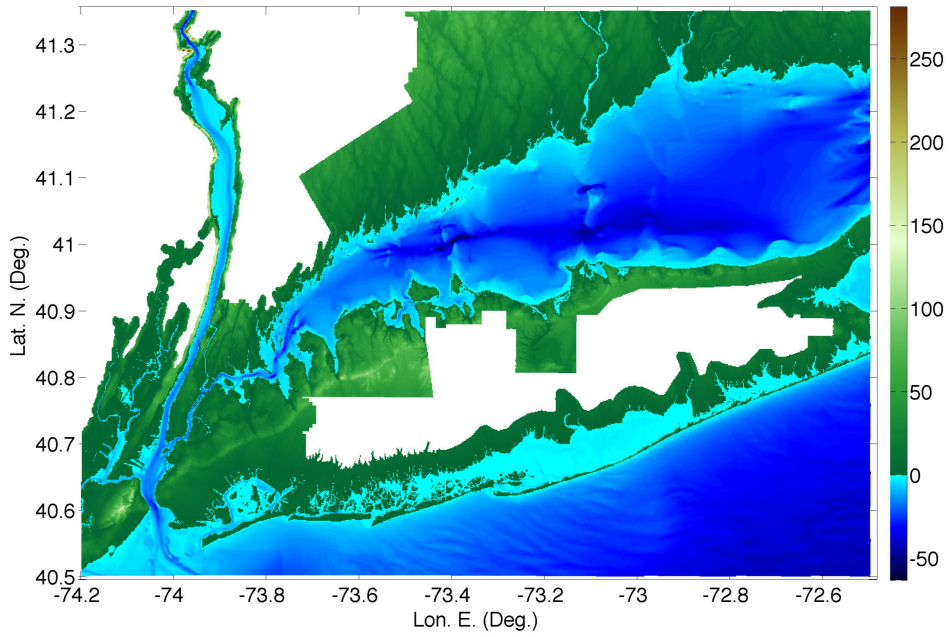

Figure 4: FEMA's 8 m DEM bathymetry/topography (FEMA, 2014) has excellent resolution in the specific area of interest, but lacks completeness for larger domains. This bathymetry was used to define the depth matrix in the finest resolution grid G1, and was combined with the 90 m NOAA DEM data to produce Grid G2 (Table 1). Color scale is bathymetry (< 0) and topography (> 0) in meters referenced to NAVD88 vertical datum.

ure 5 shows the resulting (interpolated) bathymetry and topography for grids G1 and G2. Vertical datum are referenced in all grids to NAVD88. Note that Grid G1 is oriented at 18° clockwise from north (Fig. 3). This orientation allows for a more efficient use of grid points, that significantly reduces the model computational time.

Finally, the fresh water discharge from the Hudson River is estimated to be 600 m^3/s USGS (2010), compared to a maximum tidal volume flux through the mouth of the Hudson River during a MHW tide at Manhattan Island of over 6000 m^3/s. The latter is based on current and surface elevation data computed at the mouth of the Hudson River using FUNWAVE-TVD, for tide only simulations (see details later). Because the river discharge rate is relatively small by comparison, and in order to isolate tidal effects, the river current will be neglected in this study.

3 Tide Only Modeling

The goal here is to simulate realistic tide conditions in the HRE that achieve a maximum elevation equal to the local MHW level at some selected NOAA tide gages. To do so, we first selected a period of time during which high tides with maximum elevation near the local MHW level were known to occur; this period runs from 7:00 am on July 13, 2015 to 7:00 pm on July 14, 2015. This tidal period was modeled with FUNWAVE-TVD in the 616 m resolution grid G3b, based on boundary and initial conditions (surface elevation and horizontal velocity) obtained from a large scale barotropic tide model, the "Oregon Tide Prediction Software" (OTPS). Once simulated in grid G3b, tidal forcing results were passed to the nested grids G2 and G1 (Fig. 3), following the one-way coupling method detailed before.

OTPS' latest version TPXO8 predicts surface elevations and tidal currents on a 2 arc-minute grid along the U.S. east coast. Since this type of model and the coarse discretization make it more accurate in deeper water, offshore, (Stammer et al., 2014), simulations were initiated in the larger coarser resolution domain G3b, whose boundary is mostly located in deep water. Following Tajali-Bakhsh et al.'s (2014) approach, boundary conditions were ramped-up according to a "tanh" function, from zero to the TPXO8 predictions, over nearly a half-semidiurnal tidal cycle (6 hours). Model results were then allowed to stabilize for another 12 hours in grid G3b before being specified along the boundary of grid G2 and so forth. To validate and calibrate tide

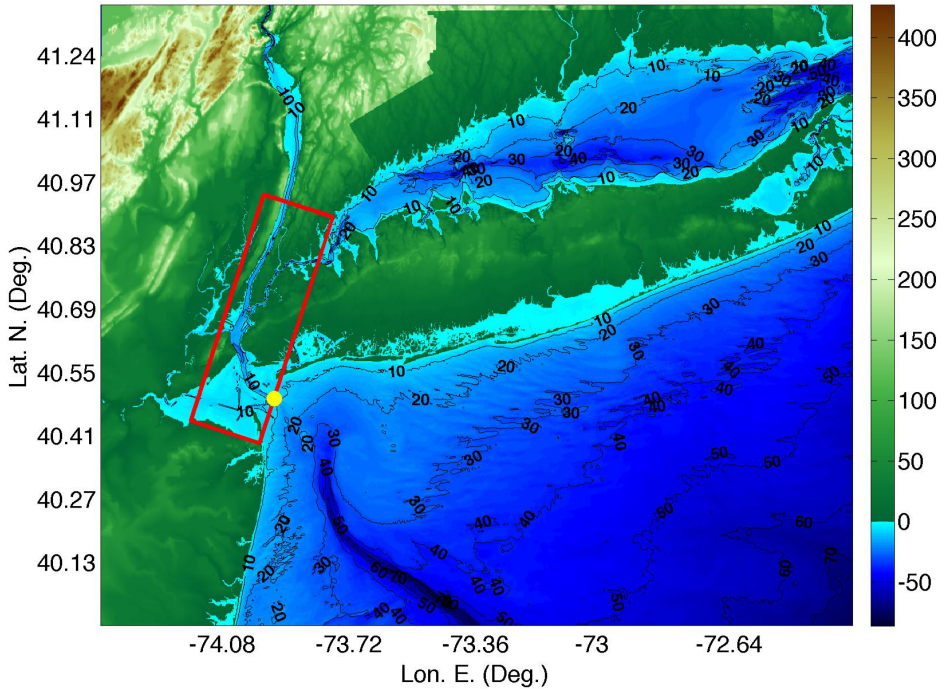

Figure 5: Model bathymetry and topography for grids G1 (red box) and G2 (footprint of the figure; Table 1), encompassing the Hudson River Estuary (HRE). Within this region we perform combined tide-tsunami simulations and compare results to tsunami simulations over a static tide level. Color scale and black contours is bathymetry (< 0) and topography (> 0) in meters referenced to NAVD88 vertical datum. Note the deep canyon offshore of the HRE mouth. The yellow bullet marks the location of the numerical gage at the entrance to Raritan Bay (-73.944 Lon. E., 40.501 Lat. N, local depth 16.9 m), where time series of surface elevations are computed in Fig. 13 for the 3 incident tsunamis.

simulations, numerical tide gage data was collected at the locations of twenty NOAA tide recording stations in the area (Table 2; Fig. 6); this includes 2 actual tide gages, at Sandy Hook and Battery Point, and 18 virtual tide gages where corrections are made with respect to the actual gages based on a harmonic analysis. At some of these virtual stations, referred to as subordinate stations (numbered #2 to #7 and #13 to #16), only maximum and minimum tide levels and their time of occurrence are predicted; at the other virtual stations, full time series are predicted. Figure 6 shows that, in the HRE, all 20 stations are located within grid G2, whereas only 14 stations are located within grid G1 (Fig. 7a). Numerical results obtained for the maximum surface elevation η_m during the second tidal cycle were compared to the predicted maximum at each station η_p, which is known to be close to the local MHW level for the selected time period. These values and their absolute and relative differences are listed for each station in Table 2, after the model friction coefficient was adjusted as detailed below.

To achieve a good agreement between tide simulations and the reference data at NOAA's tidal stations, the Manning bottom friction coefficient was adjusted in FUNWAVE-TVD's grids. A Manning coefficient of $n = 0.025$ was used throughout grid G2. In grid G1, tidal elevations modeled and predicted at NOAA's stations marked in Fig. 7, were used to calibrate bottom friction. For the Hudson and East Rivers, north of Battery Point, a Manning coefficient of $n = 0.015$ was used, while in the remainder of the grid G1 domain a Manning coefficient of $n = 0.025$ was thus used; values of the corresponding friction coefficient $C_d = gn^2/h^{1/3}$ are shown in Fig. 7d (with g the gravitational acceleration and h, here, being the local depth with respect to NAVD88); C_d values are seen to vary between 0.001 and 0.005 (with $C_d = 0.0025$ being a typical value for coarse sand). Note that, the same bottom friction values determined in the tide model will be used in tsunami simulations into the HRE.

Using the calibrated bottom frictions in grid G1, Fig. 8 shows a comparison of time series of surface elevations modeled at the 20 stations in grids G1 and G2, with NOAA's reference data (either full time series or extrema, whichever are available). Visually, the agreement between these appears to be quite good, and more so for the grid G1 results. This is confirmed in Table 2, which shows that, in grid G1, the modeled high tide water levels at 13 of the 14 stations are within 0 to 9% of NOAA's predictions, with a RMS value of 4.73%.

The largest difference is observed at the Williamsburg Bridge station, where model data is over 17% greater than NOAA's prediction; including this value, the RMS difference between modeled and predicted results over 14 stations in grid G1 becomes 6.5%. The overall agreement of model results with NOAA's predictions is better in grid G1 than in grid G2. Fig. 7b shows the envelope of computed maximum tidal elevations in grid G1, during the second tidal cycle (after model ramp-up). We see, there is little variation in maximum level (less than 0.08 m) from the mouth of the HRE to the New York harbor and the East River; as should be expected, maximum tide elevations gradually decrease in the Hudson River, from Battery Point towards upstream; and maximum elevations are larger in Long Island Sound, due to funneling effects. The average of maximum tidal elevations computed in grid G1 is +0.72 m NAVD88. For comparison, NOAA provides a tool, VDatum, that allows to approximately computed an average surface elevation for the local MHW referenced to NAVD88. This is done for grid G1 in Fig. 7c, where we see a pattern of maximum tidal surface elevations in the HRE similar to that computed with FUNWAVE-TVD. However, surface elevations are systematically smaller with the average calculated for VDatum data at +0.64 NAVD88 (with a standard deviation of 0.02 m), hence, 0.08 m below that calculated in our simulations. Such a difference, however, is deemed small and confirms the relevance of the present tidal simulations in the HRE.

Now, for the purpose of comparing dynamic tide-tsunami to tsunami over a static level simulations, we need to select a local static mean high water level throughout grids G1 and G2. For consistency, since we will use our tide simulations in the dynamic tide-tsunami simulations, this level is selected to +0.72 m NAVD88, as the average of FUNWAVE's results across grid G1. Looking at Fig. 7b , we see that this level is achieved within ±0.02 m in most of grid G1(excluding Long Island Sound, the western part of Raritan Bay, and the Upper East River). For the tsunami only simulations over a static water level, this average value was added to the bathymetry matrix, creating a geodetic vertical datum approximately referenced to MHW level. The technique of using a static water level corresponding to MHW in tsunami simulations is consistent with the methodology of Grilli et al. (2015).

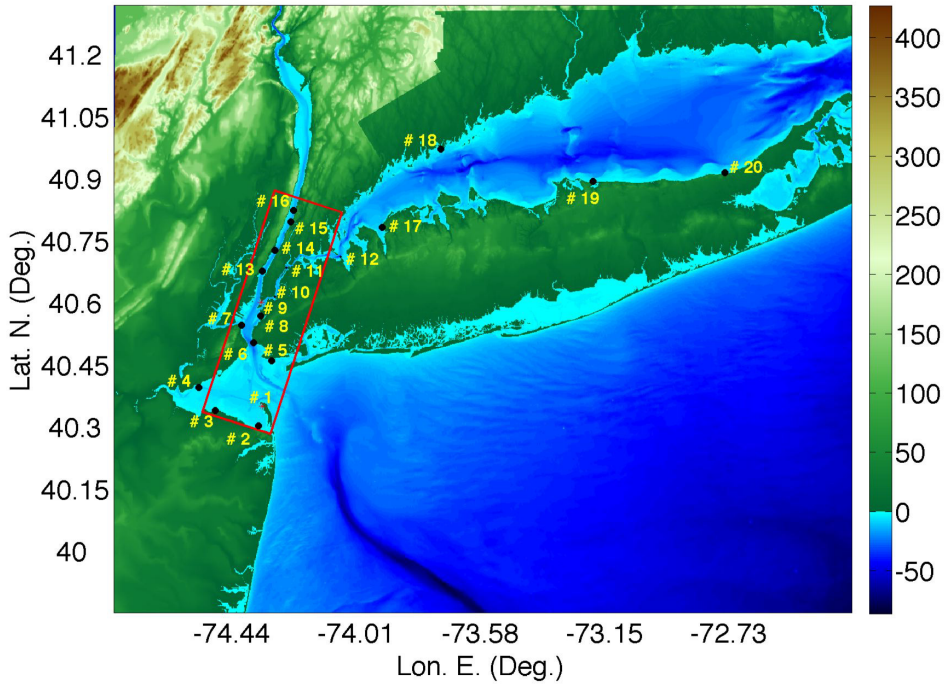

Figure 6: Footprint area of grid G2 with marked locations of 20 NOAA tide gage stations (numbered labels); the red stars indicate actual tide gages at #1: Sandy Hook and #9 Battery Point, and the black symbols mark virtual tide gages where corrections are made with respect to the actual gages based on a harmonic analysis (see locations in Table 2). The red box marks the footprint of grid G1. Computed and measured tide time series are plotted in Figure 8, and differences between these are summarized in Table 2. Color scale is bathymetry (< 0) and topography (> 0) in meters referenced to NAVD88 vertical datum.

Tide Gage Station				NOAA	Grid G2 (154 m)			Grid G1 (38.5 m)		
No.	Name	Lat. N. (Deg.)	Lon. E. (Deg.)	η_p (m)	η_m (m)	Absol. diff. (m)	Relat. diff. (%)	η_m (m)	Absol. diff. (m)	Relat. diff. (%)
#1	Sandy Hook	40.7003	-74.0135	0.71	0.78	0.07	9.42	0.73	0.02	3.24
#2	Atlantic Highlands	40.4183	-74.0200	0.72	0.78	0.06	8.58	0.74	0.02	2.56
#3	Waackaack	40.4483	-74.1433	0.72	0.82	0.11	15.25	0.78	0.07	9.37
#4	Princes Bay	40.5117	-74.2000	0.75	0.84	0.08	11.09	-	-	-
#5	Coney Island	40.5667	-73.9833	0.71	0.76	0.05	7.62	0.71	-0.00	-0.02
#6	Fort Hamilton	40.6083	-74.0350	0.73	0.80	0.07	9.14	0.71	-0.02	-3.39
#7	St. George	40.6433	-74.0733	0.66	0.78	0.11	17.19	0.72	0.05	7.79
#8	Gowanus Bay	40.6650	-74.0133	0.71	0.78	0.08	11.27	0.72	0.01	2.05
#9	Battery Point	40.4665	-74.0094	0.69	0.77	0.08	12.04	0.71	0.02	2.89
#10	Williamsburg Bridge	40.7117	-73.9683	0.59	0.72	0.13	22.73	0.69	0.10	17.44
#11	Horns Hook	40.7767	-73.9417	0.69	0.55	-0.14	-19.85	0.75	0.06	9.41
#12	Willets Point	40.7933	-73.7817	1.16	0.98	-0.18	-15.77	-	-	-
#13	Union City	40.7667	-74.0183	0.65	0.65	0.00	0.03	0.67	0.02	2.66
#14	Edgewater	40.8133	-73.9783	0.63	0.51	-0.12	-18.73	0.63	-0.01	-0.82
#15	Spuyten Duyvil	40.8783	-73.9250	0.56	0.36	-0.20	-35.52	0.58	0.01	2.18
#16	Riverdale	40.9033	-73.9167	0.58	0.33	-0.25	-42.93	0.58	-0.01	-0.91
#17	Glen Cove	40.8633	-73.6550	1.19	0.96	-0.23	-19.62	-	-	-
#18	Long Neck Point	41.0383	-73.4800	1.08	0.90	-0.18	-16.50	-	-	-
#19	Cedar Beach	40.9650	-73.0433	0.97	0.77	-0.20	-20.95	-	-	-
#20	Northsville	40.9817	-72.6450	0.81	0.62	-0.19	-22.86	-	-	-

Table 2: Definition and location of NOAA Tide Gage Stations marked in Fig. 6. The maximum water level elevation with respect to the NAVD88 datum is given at each station for the NOAA high tide (MHW) prediction η_p, compared to surface elevation η_m modeled with FUNWAVE-TVD in the 154 m resolution grid G2 and 38.5 m resolution grid G1 (note, only 14 stations are located within this grid); the absolute $(\eta_m - \eta_p)$ and relative differences between these $((\eta_m - \eta_p)/\eta_p)$ are listed for each grid.

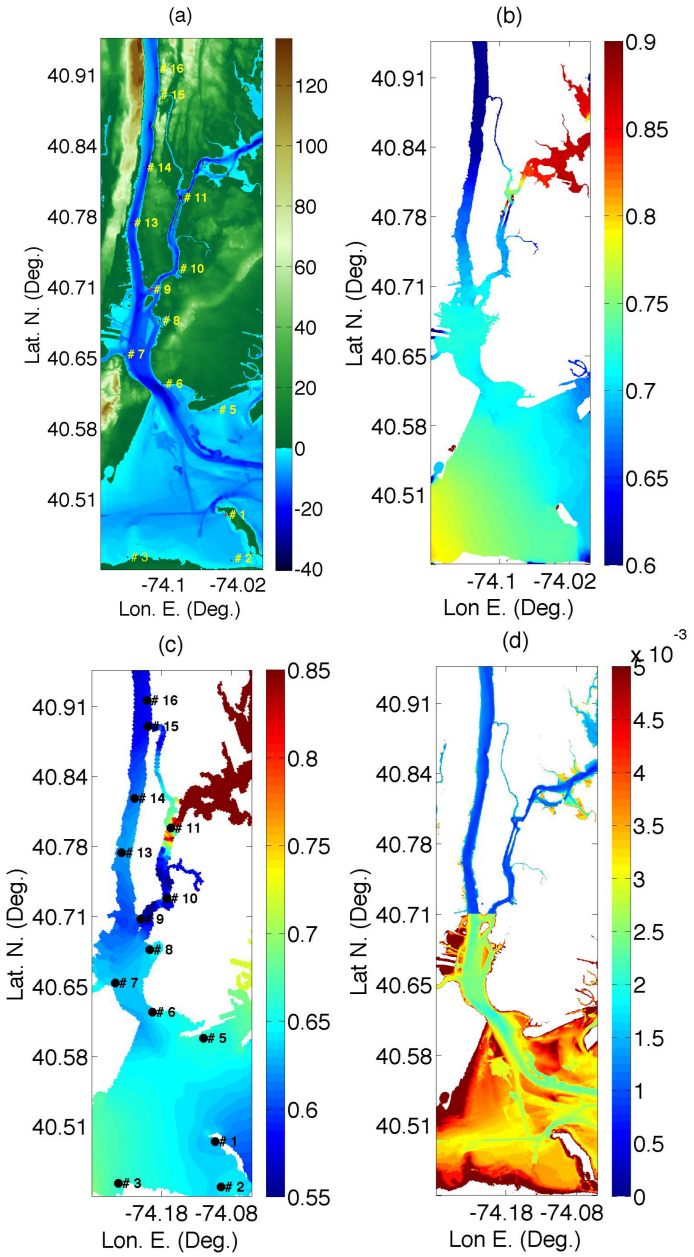

Figure 7: Tide simulations in grid G1 (a,b,c; color scale in meters from NAVD88 datum): (a) bathymetry with marked NOAA tide stations (symbols/numbers; see Fig. 8 and Table 2 for NOAA 's predicted and modeled elevations); (b) envelope of maximum computed tidal elevations; (c) Local MHW calculated by VDatum; (d) friction coefficient C_d; a Manning coefficient $n = 0.025$ was used throughout the domain except in the rivers, where a value $n = 0.015$ was used.

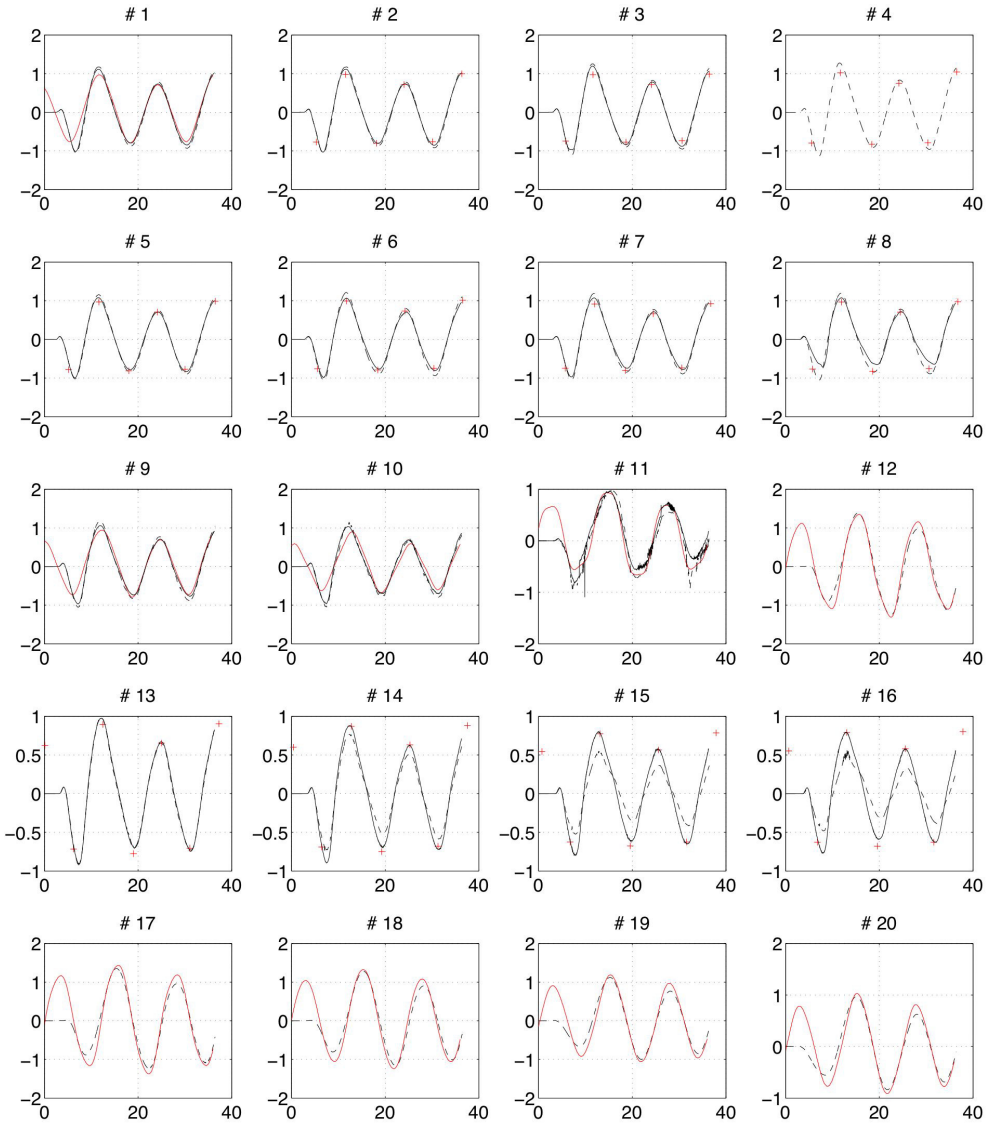

Figure 8: Time series of tide surface elevation (with respect to NAVD88) computed with FUNWAVE-TVD at the locations of 20 NOAA tide gage stations (Table 2; Figs. 6 and 7a), in grid G1 (solid black) and G2 (dash black), compare to NOAA's reference data (solid red; either full time series or extrema, whichever are available), for tides during the period 7:00 am on July 13, 2015 to 7:00 pm on July 14, 2015. The model is initialized in grid G3b with tide results computed in OTPS' model TPXO8. The Manning bottom friction coefficient is calibrated in grids G1 and G2 to achieve a good agreement (Fig. 7d). Table 2 compares maximum water level values during the second tidal cycle, which correspond to to the local MHW level.

4 Tsunami Only Modeling

Based on earlier NTHMP work summarized above, three tsunamis were propagated into the HRE, due to a: (i) a far-field M_w 9 seismic source in the Puerto Rico Trench (PRT) (Grilli et al., 2010, 2013b); (ii) a far-field source from a 80 km^3 partial collapse of the western flank of the Cumbre Vieja Volcano (CVV) in La Palma, Canary Island, deemed the likeliest extreme collapse scenario (Abadie et al., 2012; Tehranirad et al., 2015); and (iii) a near-field submarine mass failure (SMF) modeled as a Currituck (CRT) slide proxy on the continental slope off of the Hudson River canyon (Grilli et al., 2015). The far-field tsunami sources (PRT, CVV) are specified and their propagation first modeled in grid G4 (Fig. 1), where boundary conditions to continue simulations in grid G3b are computed. The near-field tsunami source (CRT SMF proxy) is specified and its propagation first modeled in grid G3a (Fig. 2).

Figure 9a shows the initial surface elevation of the M_w 9 PRT tsunami source computed with Okada's method (Okada, 1985), based on 12 SIFT sub faults (Grilli et al., 2013b; Gica et al., 2008). Figs. 9b,c,d then show then show instantaneous surface elevations computed in the large ocean basin scale 1 arc-min resolution grid G4 with FUNWAVE-TVD (truncated here at Lon. E. -55 for more efficiency due to the tsunami directionality), after t = 30 min, 1h 42 min and 3 h 20 min of propagation. Results show that the maximum tsunami elevations are quite directional south-to-north and focus on the upper U.S. east coast; this was already pointed out by Grilli et al. (2010). After 200 min of propagation, the tsunami is entering the SE corner of grid G3b (Fig. 3).

Figures 10a,b show the initial surface elevation and horizontal velocity magnitude for the 80 km^3 CVV flank collapse source computed by Abadie et al. (2012), at t = 20 min into the event. At this time, surface elevations reach up to 30 m, but are larger in a direction between 15 and 30 deg. south of West, as already pointed out in other work (Abadie et al., 2012; Tehranirad et al., 2015). Figs. 10c,d then show instantaneous surface elevations computed in the large ocean basin scale 1 arc-min resolution grid G4 with FUNWAVE-TVD, after t = 4 and 8 h of propagation. These results confirm that the maximum tsunami elevations are quite directional in a more or less WSW direction towards the Caribbean Islands and South America. Nevertheless, after about 8h of propagation significant tsunami waves of 2-3

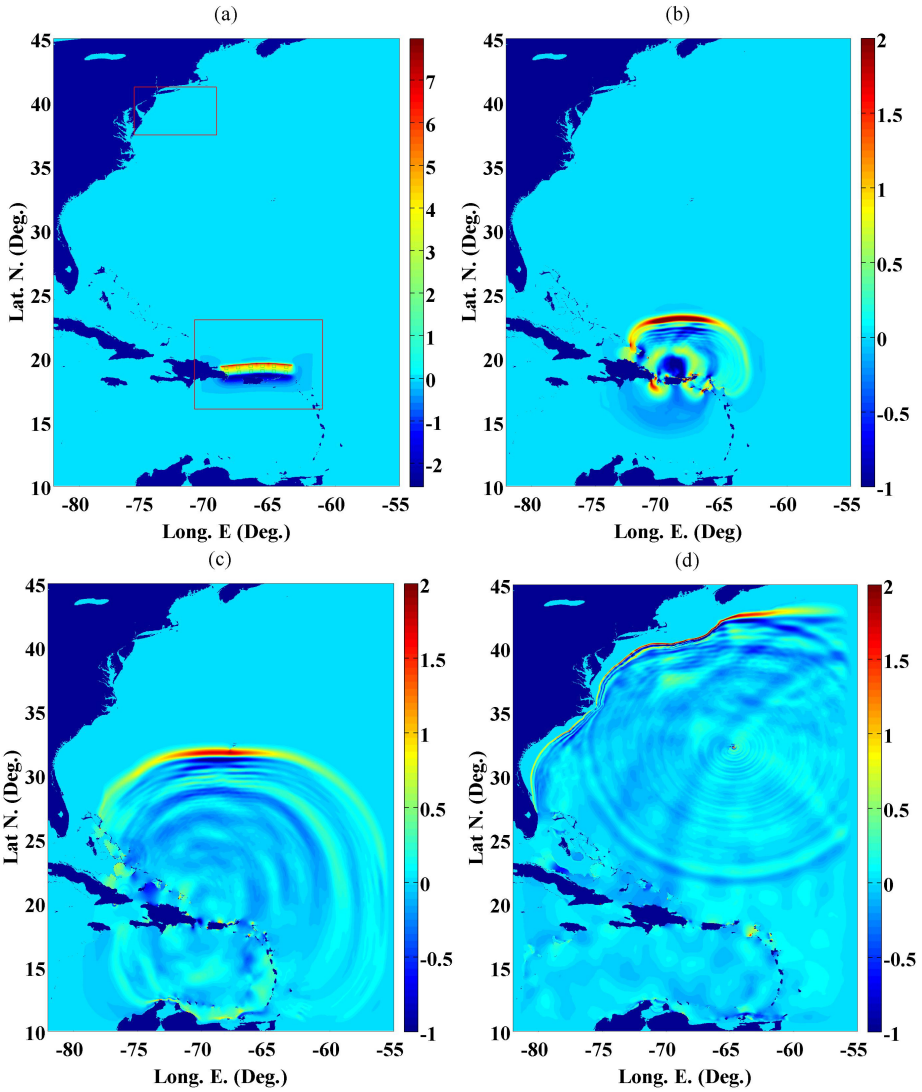

Figure 9: Large scale simulations with FUNWAVE-TVD of the M_w 9 PRT seismic source in grid G4 (truncated at Lon. E. -55; Fig. 1): (a) Initial surface elevation of tsunami source computed in lower red box with Okada's method (Okada, 1985), based on 12 SIFT sub faults (Grilli et al., 2013b; Gica et al., 2008); the upper red box approximately represents the area of Fig. 3; (b,c,d) Instantaneous surface elevations computed after t = 30 min, 1h 42 min and 3h 20 min of propagation. All color scales are surface elevation in meters.

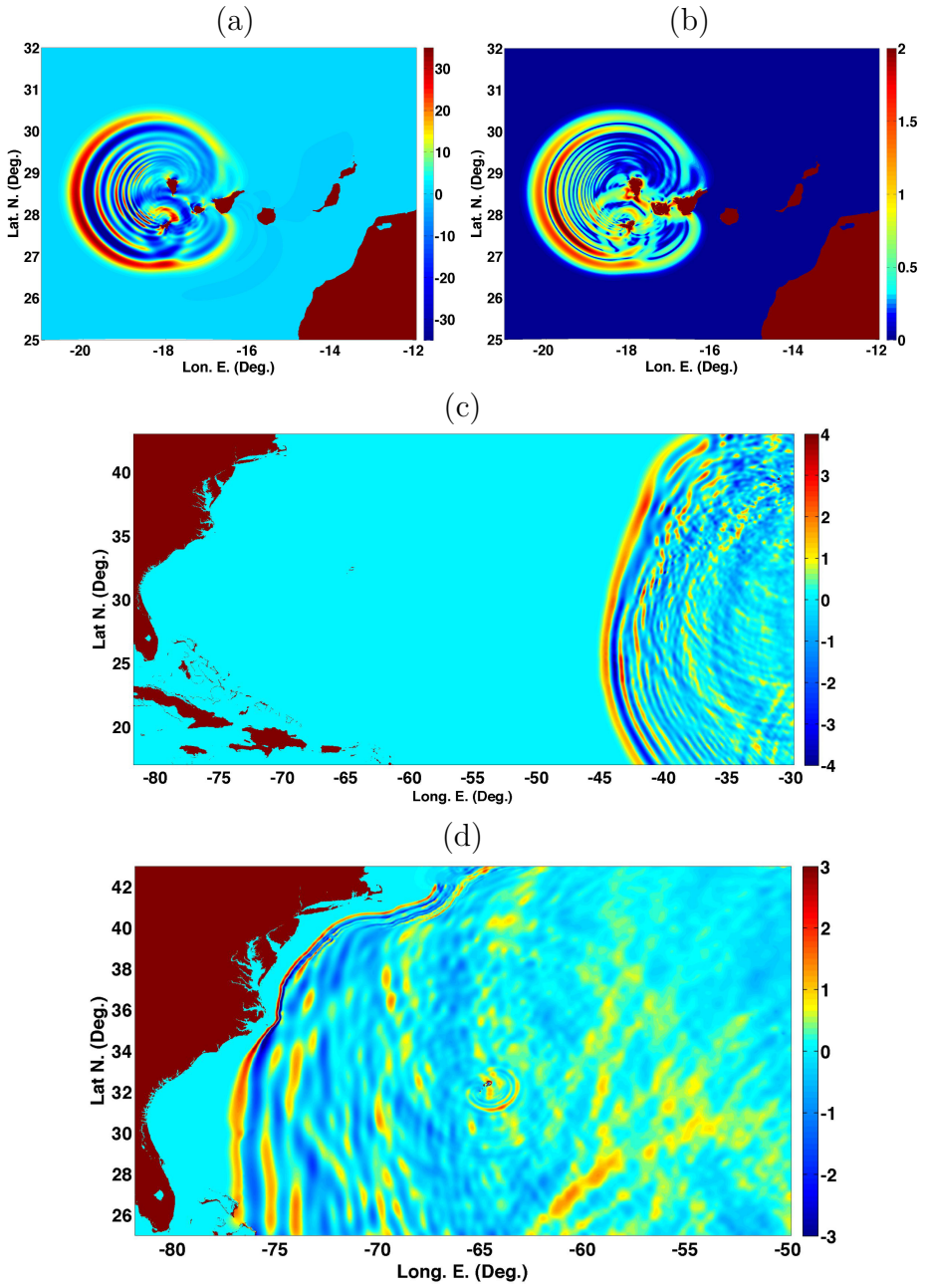

Figure 10: Large scale simulations with FUNWAVE-TVD of the 80 km^3 CVV flank collapse source in grid G4 (Fig. 1): (a,b) Initial surface elevation (m) and horizontal velocity module (m/s) of tsunami source at $t = 20$ min into the event, computed by Abadie et al. (2012); (c,d) Instantaneous surface elevations computed after $t = 4$ and 8 h of propagation into the event (color scales are surface elevation in meters).

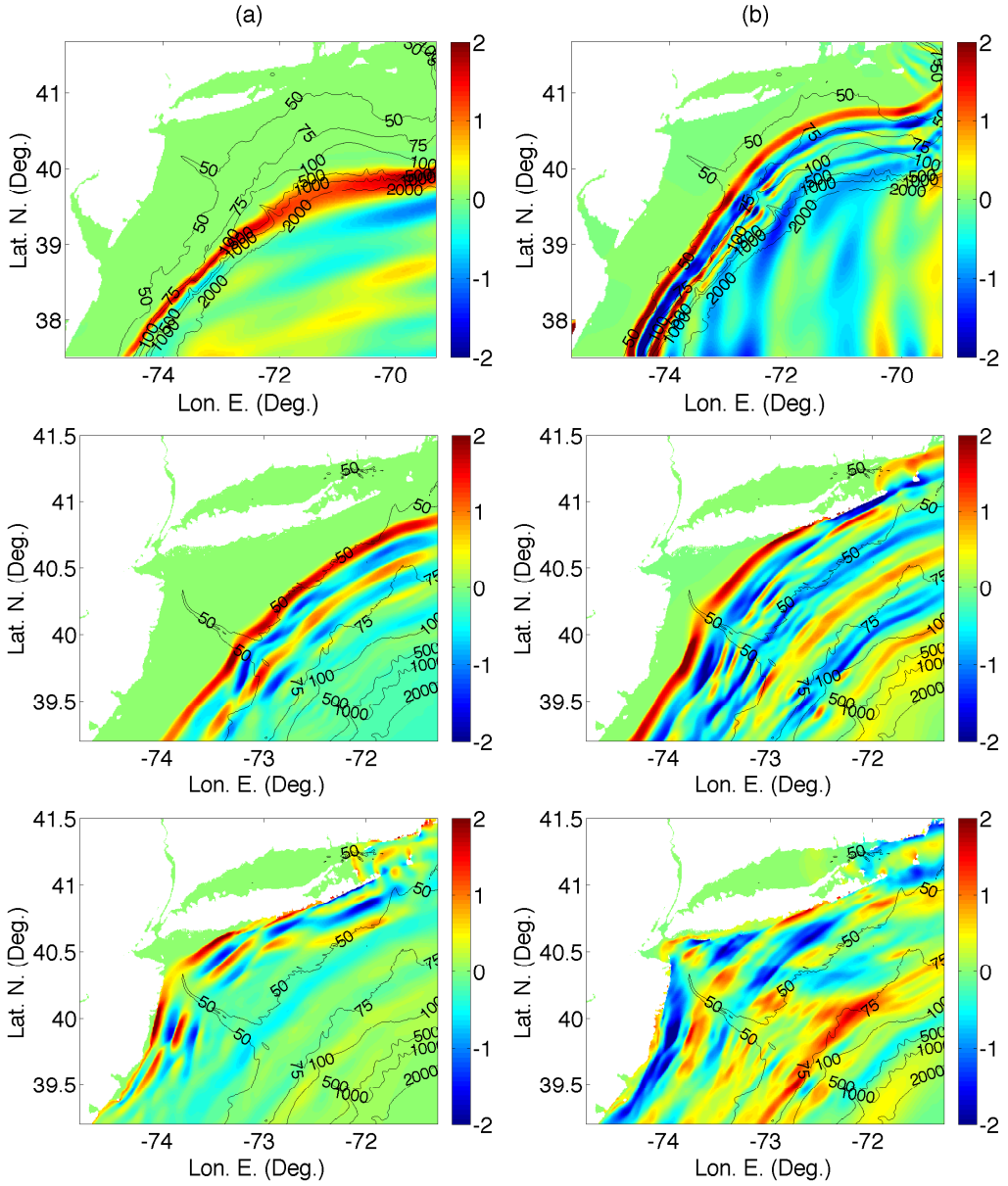

Figure 11: Computations of far-field tsunami sources with FUNWAVE-TVD. Instantaneous surface elevation in grid G3b (color scale is elevation and black contour bathymetry, both in meter), upon reaching the continental shelf, for the: (a) PRT tsunami at $t = 3$, 4 and 5h and (b) CVV tsunami at $t = 8$, 9 and 10h, since the event, from top to bottom.

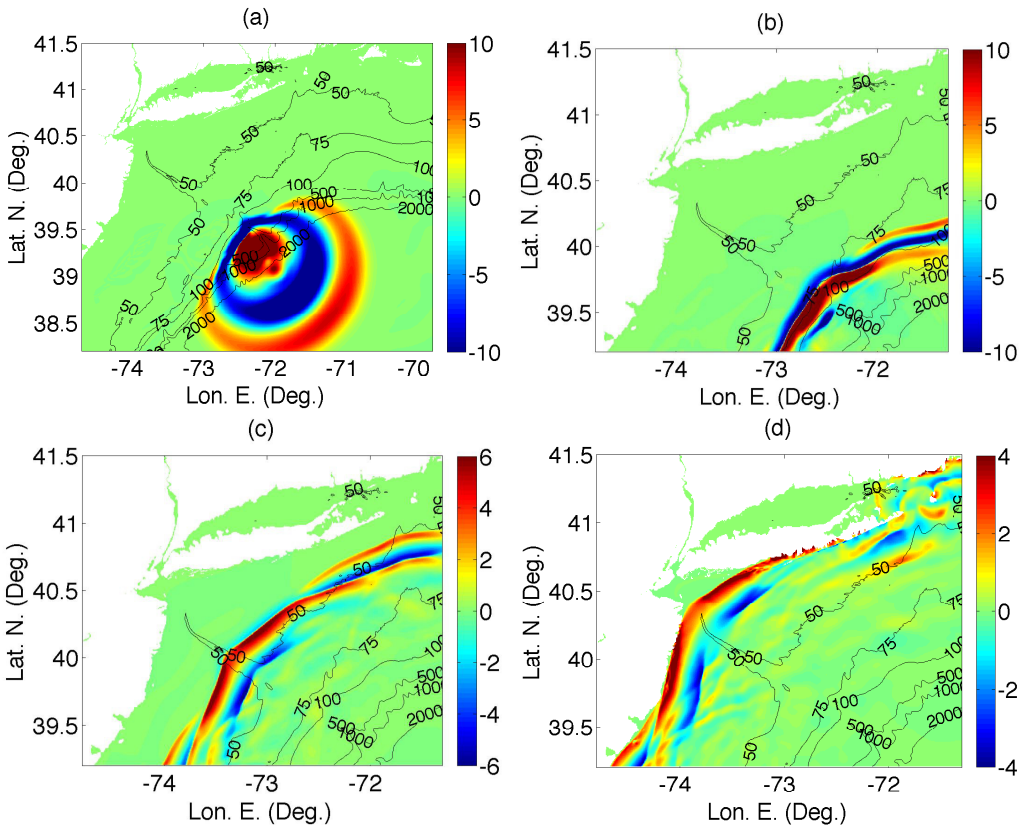

Figure 12: Computations of near-field Currituck (CRT) SMF proxy source (located in Study Area 1 (Fig. 2), off of the Hudson River canyon) with FUNWAVE-TVD (b to d); the SMF tsunami generated with NHWAVE (Ma et al., 2012; Grilli et al., 2015) is shown in panel (a) and is used as the source of FUNWAVE-TVD simulations. Instantaneous surface elevation in grid G3a (color scale is elevation and black contour bathymetry, both in meter) at $t =$ (a) 13 min, (b) 30 min, (c) 1h 18 min and (d) 2h 8 min into the event.

m elevation reach the upper U.S. east coast, entering the SE corner of grid G3b (Fig. 3).

Details of the arrival of the 2 far-field tsunamis, PRT and CVV, are shown in Fig. 11a,b, in the form of instantaneous surface elevations computed at $t = 3$, 4 and 5h, and 8, 9 and 10h (since the event, respectively, starting at a time when the tsunamis are about or starting to propagate over the continental shelf in grid G3b. At this stage, due to refraction, the leading tsunami waves appear to be more or less parallel to local isobaths; hence, the very different initial directionality of these tsunamis (i.e., approximately from south to north for PRT and east to west for CVV) has been lost. This property of long wave refraction was analyzed in more details by Tehranirad et al. (2015), who performed simple ray tracing analyses of the CVV tsunami and showed the strong bathymetric control of nearshore propagation, leading tsunami waves to focus or defocus towards specific areas of the coastline. In particular, we see that, in both cases, incident waves refract away from the Hudson River canyon and focus on the shores of eastern New Jersey and western Long Island (NY). Partial wave reflection occurs along these shores and reflected waves interact later in time with waves in the incident wave trains to create more complex patterns of shore (see, e.g., Fig. 11b bottom panel).

Figure 12a shows the surface elevation for the near-field Currituck (CRT) SMF proxy source, interpolated in the 616 m resolution grid G3a, at $t = 13$ min into the event. This source was computed using the three-dimensional non-hydrostatic model NHWAVE (Ma et al., 2012; Grilli et al., 2015) and corresponds to the CRT SMF proxy located in Study Area 1 (Fig. 2) off of the Hudson River canyon. FUNWAVE-TVD simulations were initialized in grid G3a with this source's elevation and corresponding horizontal velocity (not shown here). At this time, the CRT tsunami waves have a large leading depression wave (-10 m) moving into the Hudson River Canyon, followed by a larger (15 m) elevation wave. Other waves in the wave train are propagating offshore (to the SE); upon propagation (not shown here), these shorter dispersive waves develop oscillatory tails of higher frequency waves. The onshore propagation of the the CRT tsunami is detailed in Figs. 12b-d, which show instantaneous surface elevations computed at $t = 30$ min, 1h 18 min and 2h 8 min into the event. Similar to the PRT and CVV cases, the shelf bathymetry induces a strong refraction of incoming tsunami waves, which gradually become parallel to local isobaths as they approach shore; as for the other two cases, waves are

refracted away from the Hudson River Canyon to focus on the shores located on either sides of it, where partial reflection occurs.

Simulations of the propagation of the 3 incident tsunamis (PRT, CVV, CRT) towards and into the HRE are pursued in the nested grid G2 with FUNWAVE-TVD, by one-way coupling, using results obtained in grids G3a,b as boundary conditions, and then similarly into grid G1 (Figs. 3, 6 and 7a); as indicated before, coupling occurs by way of time series of boundary conditions for the surface elevation and velocity along the boundary of each finer grid, computed in each coarser grid. Simulations are first performed here for a static reference level equal to the local averaged MHW level in grid G1, +0.64 m NAVD88, and then these will be performed dynamically, in combination with the calibrated tide, by superimposing tide and tsunami time series along the boundary of grid G2 (see next Section).

Figure 13 shows time series of computed surface elevations, relative to the static water level, for the three incident tsunamis, at a numerical gage located at the entrance of Raritan Bay along the eastern boundary of Grid 1 (-73.944 Lon. E., 40.501 Lat. N, local depth 16.9 m; see location in Fig. 5); for comparison, similar time series are plotted at a gage located on the SE corner of grid G2, in deeper water of 78 m depth (Table 1). At this location, the PRT tsunami wave train has a leading crest and features 2 larger waves (with maximum elevation of about 2 and 1 m, respectively, and an 18 min period) and a tail of smaller oscillations. By contrast, the CVV tsunami wave train, which also has a leading crest, features more than 6 larger and longer waves (of maximum elevation about 1.8 m and period 21 to 42 min), over which many shorter wavelength (higher frequency) waves are superimposed (with period 4 to 6 min), as a result of dispersion (Tehranirad et al., 2015). Finally, because of the proximity to the source (Fig. 12a), the CRT SMF proxy tsunami at grid G2's SE corner appears as a large dipole wave of 6.5 min period with a leading depression of -9 m followed by a 12 m crest.

After propagating over the shallow shelf to Raritan Bay's entrance, at the numerical gage located on grid G1 boundary in the middle of the HRE (Fig 5), about 1h 45 min later for each tsunami, each of these wave trains has significantly transformed, with wave elevations decreasing and some waves being damped out. This results from the combination of energy spread out, due to wave refraction over the Hudson River Canyon bathymetry, and energy dissipation due to bottom friction; the former was confirmed by wave ray tracing in this

area and the latter by a comparison with an analytical solution, both detailed in Tehranirad et al. (2015). Hence, upon entering the HRE, maximum surface elevation for the PRT, CVV and CRT tsunamis are reduced to 0.8, 1.2 and 2 m, respectively.

Figure 14 shows envelopes of maximum surface elevation computed in grid G1 for the three incident PMTs, over the +0.64 m NAVD88 static level. For each tsunami, these are found to be consistent with the surface elevations computed at the entrance to the HRE (Fig. 13). For PRT, maximum coastal elevations/runup within the HRE are 1 to 2 m, and for CVV these are 1.3 to 2.5 m; for CRT, surface elevations are divided into 2 regions within the HRE: (i) outside of New York Harbor, coastal inundation/runup is 2 to 3 m in most areas; but (ii) inside the harbor maximum coastal elevations within the HRE are 1.5 to 2 m.

5 Dynamic Tide-tsunami Simulations

Simulations are now repeated for the three incident PMTs, in combination with a time varying tide-induced mean sea level. The tide was calibrated earlier for its maximum amplitude to closely match the MHW level in the area of grid G1. To maximize inundation, various phases of the tide at the time of tsunami arrival will be considered.

In deeper water, both tide and tsunamis are long waves of fairly small amplitude, as compared to depth and wavelength, which can thus be linearly combined (both elevation and current) (Dean and Dalrymple, 1991). For such a superposition to be accurate closer to shore, however, water depth must be large enough, perhaps on the order of 20 m or greater in the present case, considering incident tsunami amplitudes are on the order of 2 m or less (Fig. 13), and tide amplitudes are on the order of 1 m or less (Fig. 8). Here, incident tides computed in grid G3a and tsunamis computed in grid G3b are linearly combined along the offshore boundary of grid G2 (Fig. 5), which is located in water depths greater than 30 m, except for small areas on the northernmost part of its eastern boundary, in Long Island, and the easternmost part of its southern boundary in New Jersey. However, as these are fairly small parts of the grid boundary located far away from the entrance to the HRE (Fig. 5), nonlinear effects that might arise from a linear superposition of tide and tsunami signals in shallower depth parts of the boundary, are deemed negligible. For each considered tsunami-tide combination, once computations are completed in

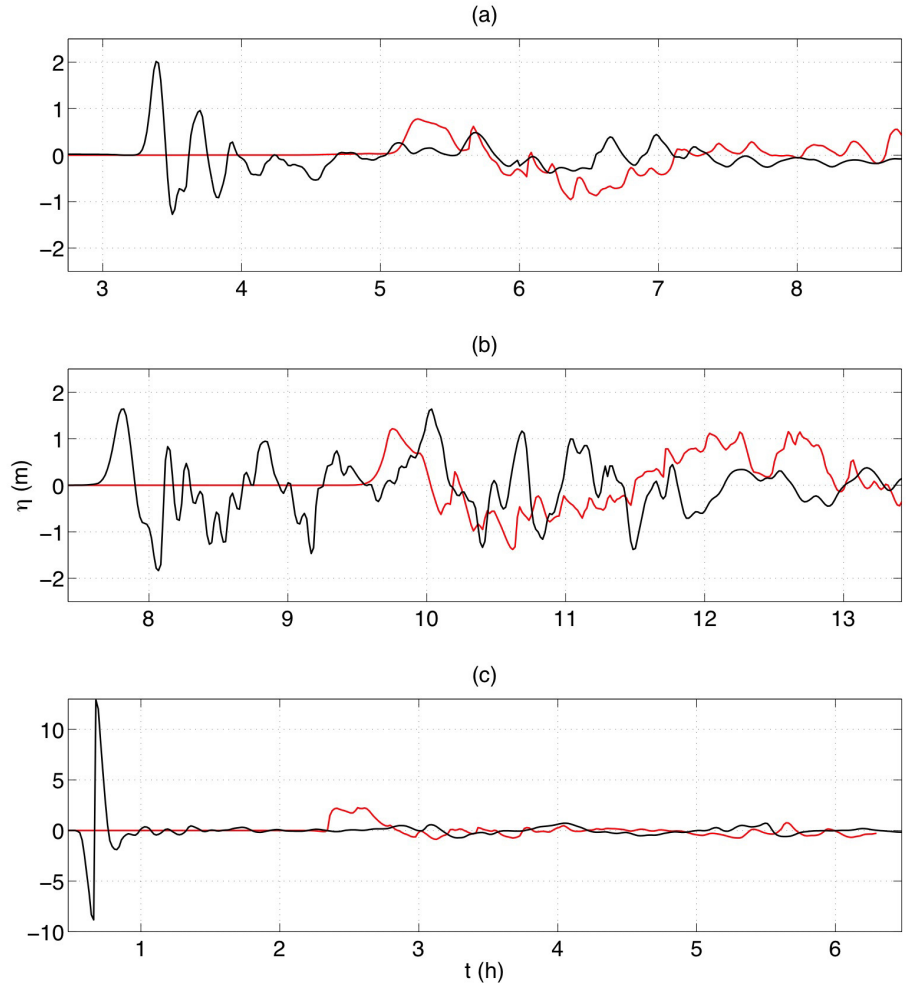

Figure 13: Time series of surface elevations computed with FUNWAVE TVD (time is from the start of each respective event): (red solid lines) at the entrance of Raritan Bay along the eastern boundary of grid G1 (-73.944 Lon. E., 40.501 Lat. N.; see location in Fig. 5), and (black solid lines) at the SE corner of grid G2 (Table 1), for the propagation of each incident PMT, over a +0.64 m NAVD88 static level (approximating the local MHW level): (a) PRT ; (b) CVV; and (c) CRT SMF proxy.

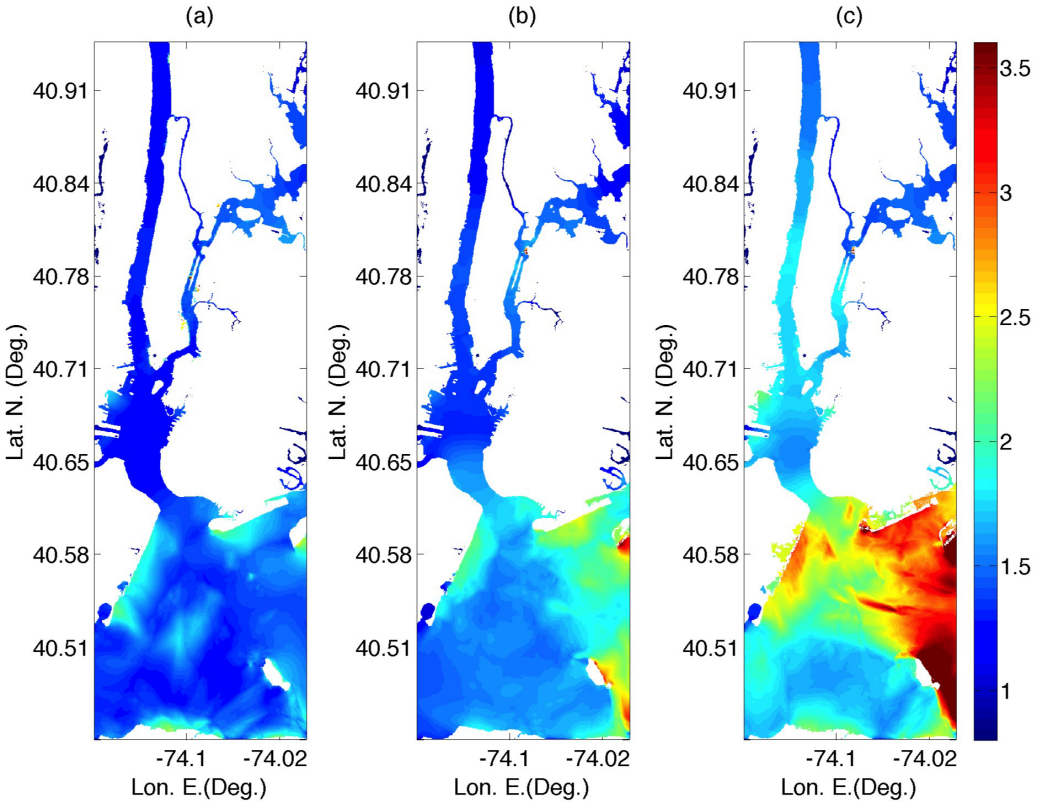

Figure 14: Envelope of maximum surface elevation (color scale in meter) computed with FUNWAVE-TVD for the propagation of each incident PMT into grid G1, over a +0.64 m NAVD88 static level (approximating the local MHW level): (a) PRT (up to $t = 9$ h); (b) CVV (up to $t = 13.5$ h); and (c) CRT SMF proxy (up to $t = 6.5$ h). Times in parenthesis indicate the total time of tsunami simulations since the start of each respective event.

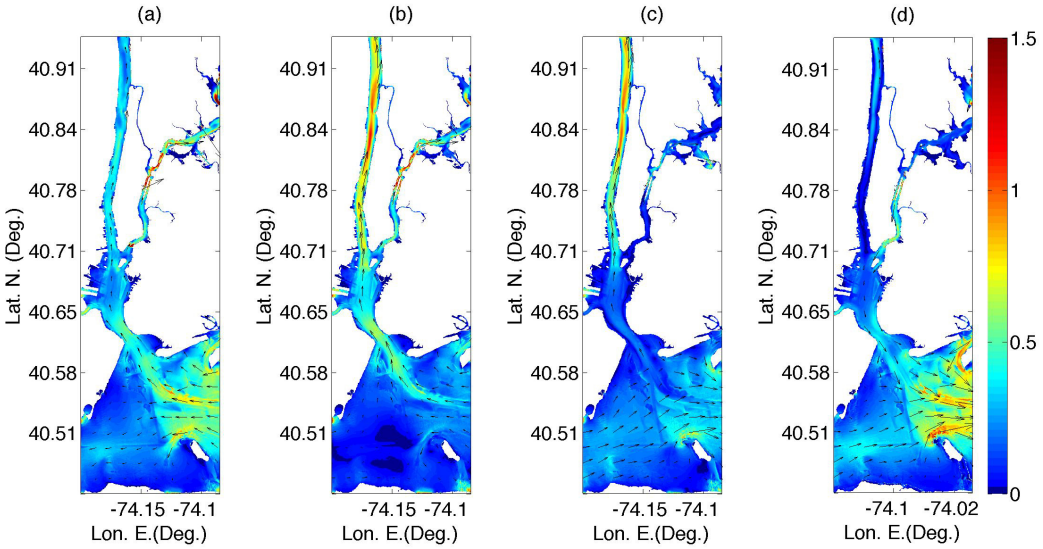

Figure 15: Magnitude (color scale in m/s) and direction (vectors) of tidal currents computed with FUNWAVE-TVD for 4 phases of the calibrated tide that causes MWL at the highest tide elevation, in grid G1; phases corresponds to the tide arriving at the Sandy Hook station #1 (Table 2; Fig. 6): (a) 1.5 h before; (b) concurrent with; (c) 1.5 h after; and (d) 3 h after high tide.

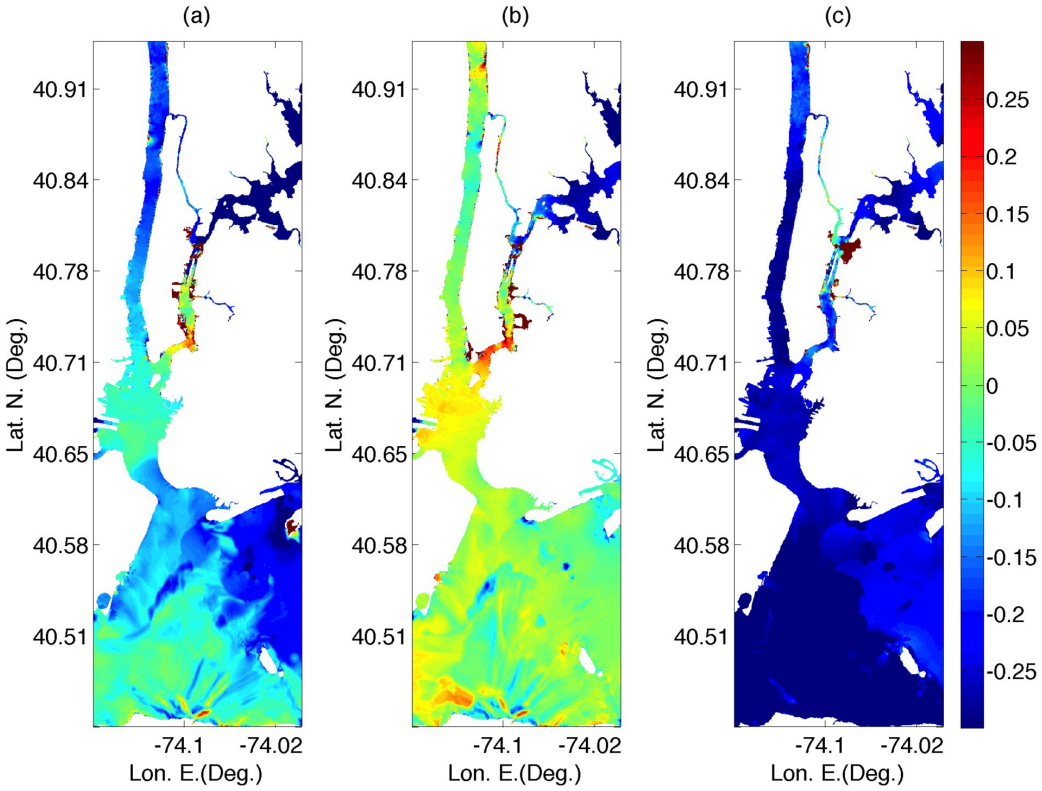

Figure 16: Difference between envelope of maximum surface elevation (color scale in meter) for the PRT tsunami modeled in grid G1, over a dynamic and static (+0.64 m NAVD88) tide level; the initial tsunami crest arrives at the Sandy Hook station #1 (Table 2; Fig. 6): (a) 1.5 h before; (b) concurrent with; and (c) 1.5 h after high tide.

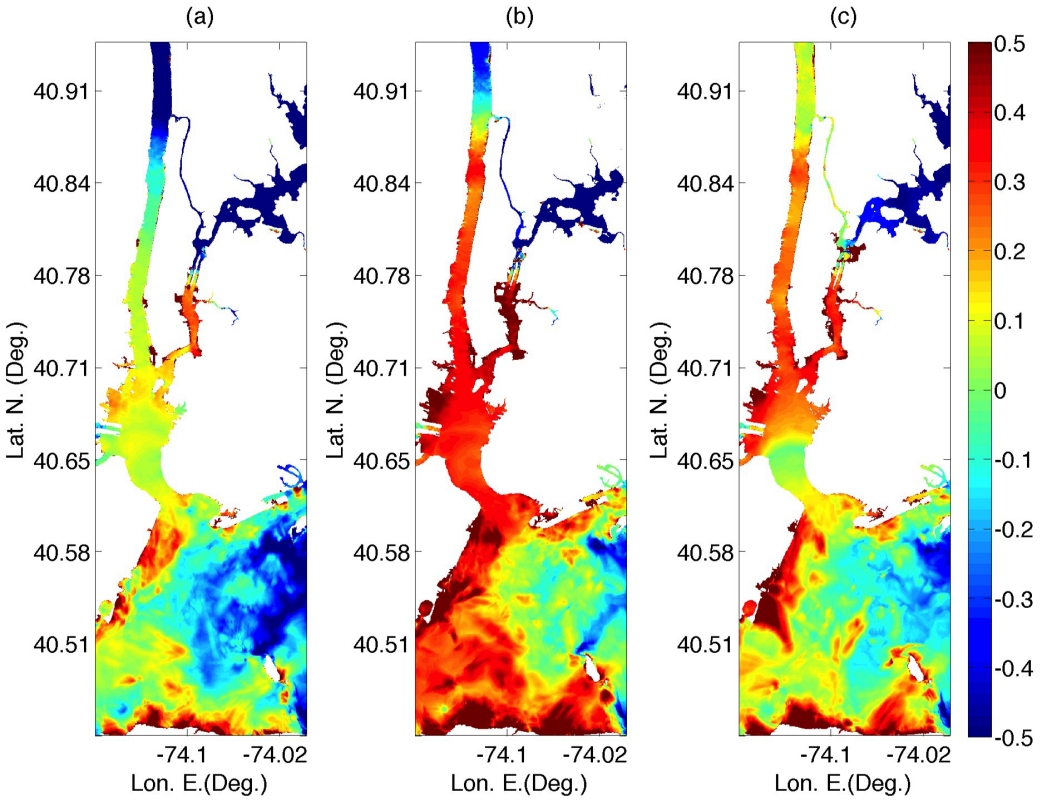

Figure 17: Same as Fig. 16 for the CVV tsunami.

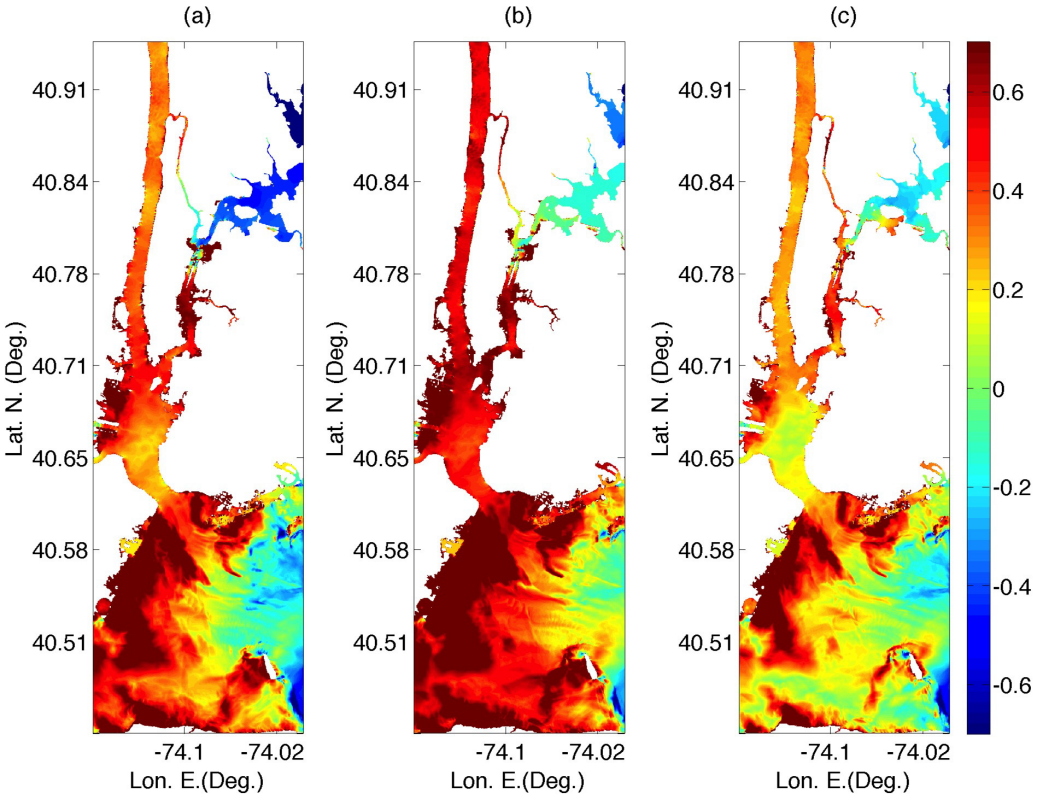

Figure 18: Same as Fig. 16 for the CRT SMF proxy tsunami.

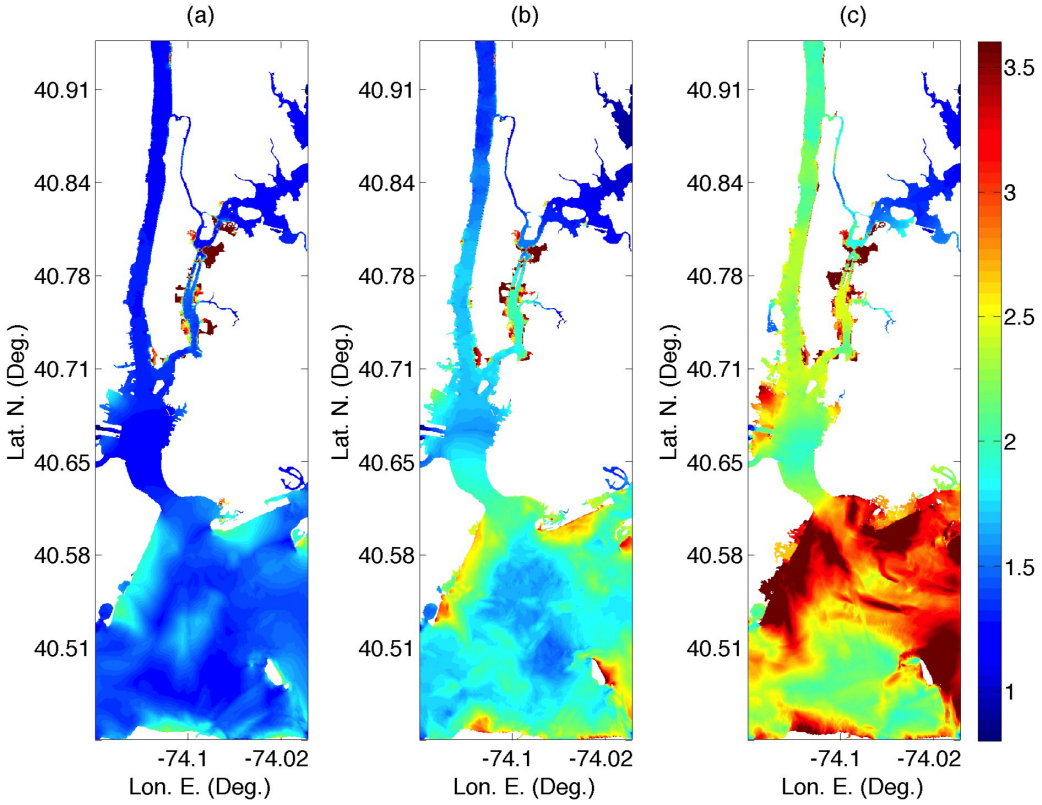

Figure 19: Envelope of maximum surface elevation (color scale in meter) computed with FUNWAVE-TVD for the propagation of each incident PMT into grid G1, over a dynamic tide (approximating the local MHW level at its highest elevation), over the 4 tide phases tested (arriving at Sandy Hook station #1 (Table 2; Fig. 6) 1.5 h before, concurrent with; 1.5 h after, and 3 h after high tide): (a) PRT (up to $t = 9$ h); (b) CVV (up to $t = 13.5$ h); and (c) CRT SMF proxy (up to $t = 6.5$ h). Times in parenthesis indicate the total time of tsunami simulations since the start of each respective event.

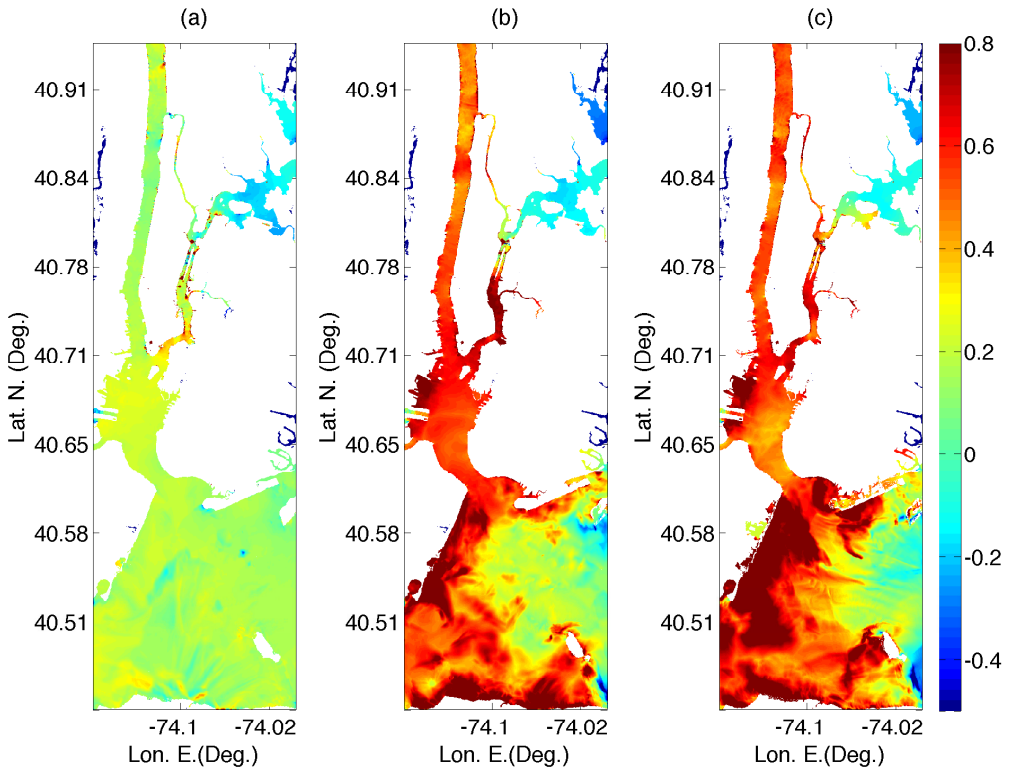

Figure 20: Difference of maximum surface elevation (color scale in meter) over grid G1 for the: (a) PRT; (b) CVV; and (c) CRT tsunamis, between the envelope of dynamic tide computations (envelope of envelopes for the 4 tide phases tested; Fig. 19) and of static tide computations (+0.64 m NAVD88 tide level; Fig. 14).

grid G2, these are pursued in grid G1 by one-way coupling as done in the previous section for the tsunami simulations over a static water level. All simulations are performed using the same Manning friction coefficients as those obtained through calibration in the tide only simulations.

The linear tide-tsunami combinations are specified on the boundary of grid G2 for a series of phases of the same tidal signal, i.e., multiple simulations are performed for each incident tsunami in order to achieve the maximum surface elevation in grid G1. Specifically, tide-tsunami combinations were selected such that the incident crest of each tsunami arrived at Sandy Hook, NJ (Station #1 in Figure 7): (i) 1.5 hours before; (ii) concurrent with; (iii) 1.5 hours after; and (iv) 3 hours after high tide. The 1.5 hour time interval between each combination represents roughly one-eighth of the dominant tidal period. [Other longer intervals were tested by Tajali-Bakhsh et al. (2014) for Chesapeake Bay, but did not result in increased nonlinear effects.] The goal of the multiple phases is to identify the combination of tidal elevations and currents that best enhances the incident tsunamis and causes the maximum combined tsunami-tide elevations and coastal inundation in the HRE. Figure 15 shows the magnitude and direction of tidal currents for the 4 selected phases of the calibrated tide. Panel (a), 1.5 h before high tide, corresponds to the strongest currents flowing into the HRE. At high tide, in panel (b), weaker currents are still flowing into the HRE, the Hudson and East Rivers, with currents being larger in the central channel. In panel (c), 1.5 h after high tide, while strong currents are still flowing into the Hudson River, the East River is at slack, and strong currents are ebbing out of the HRE. Finally, in panel (d), 3 h after high tide, currents are flowing out of the HRE and both rivers, and are strongest at the mouth of the HRE. In this simulation, the strongest currents nearly reach 1.5 m/s (3 knots), which is notably larger (more than twice) than currents that were simulated (and observed) by Tajali-Bakhsh et al. (2014) in the wider Chesapeake Bay and even in the James River.

In view of these current patterns, one might anticipate that the second and third phases of dynamic tide-tsunami simulations, in which the largest wave in each incident tsunami reaches the Sandy Hook gage, near the mouth of the HRE, concurrently or 1.5 h after high tide, should lead to the maximum amplification of the incident tsunamis. Indeed, while tidal elevations are either maximum or have not yet decreased too much from their highest level, the tsunamis propagating

into the HRE will be facing opposite (ebbing) currents that will be increasing or be already quite strong (0.5 to 0.75 m/s in Fig. 15c); these ebbing currents will keep getting stronger as the tsunamis propagate into the New York Harbor and the Hudson and East Rivers (as seen in Fig. 15c and d); these opposite currents should cause the tsunami surface elevation to rise. In Fig. 15d, while currents are even stronger 3 h after high tide, tidal surface elevations are starting to become negative and hence it will be harder to achieve higher elevations in the combined results. Although we will keep computing this fourth phase to establish envelopes, its results will not be further detailed.

Because tide and tsunami are long waves, without nonlinear interactions between these, each wave should be propagating at the same phase speed in the HRE and the combined tide-tsunami level evolve in a similar way. However, nonlinearity will affect these features, by causing amplitude dispersion effects, that will move the maximum combined elevation ahead or behind the initially combined value, as well as amplification of the tsunami elevation by opposite (ebbing) currents and vice versa.

Results of each dynamic tide-tsunami simulation will be compared to those of the corresponding simulation done over a static water level equivalent to the local MHW (+0.64 m NAVD88), in order to illustrate and quantify nonlinear effects that may occur. In addition to comparing time series of surface elevation and current at selected reference points (both in the time and frequency domain), maximum surface elevations will be compared across the computational domain.

Thus, Figures 16, 17 and 18 show differences of maximum envelopes of surface elevations computed for the dynamic tide-tsunami simulations and the static MHW level, for the PRT, CVV and CRT tsunamis, respectively. Results are shown for dynamic combinations corresponding to three tidal phases: (i)1.5 h before; (ii) concurrent; and (iii) 1.5 h, after high tide. For PRT, Fig. 16 shows that the worst case scenario regarding coastal flooding is when high tide and maximum tsunami elevation occur concurrently at Sandy Hook station, leading to increased flooding of 0.05 to 0.15 m up to Battery point. Along southern Manhattan and in the East River, for this and the two other tide phases, flooding increases by more than 0.2 m for the dynamic case, likely due to ebbing tidal currents in the river, as discussed above. For CVV, Fig. 17 shows that the worst case scenario regarding coastal flooding is also when high tide and maximum tsunami elevation occur concurrently at the Sandy Hook station, lead-

ing to increased flooding of 0.2 to 0.5 m up to Battery point. For all tide phases, we again see increases in flooding along southern Manhattan and in the East River, but here also in the Hudson River up to northern Manhattan, likely due to ebbing currents at the time the tsunami and the high tide are propagating up the HRE (more details of currents in the rivers will be presented later). Finally, Fig. 18 shows that the largest increases in coastal flooding due to dynamic tide-tsunami interactions are observed for the CRT case, for the same tide phases, with increased flooding of 0.1 to over 0.8 m both inside and outside NY harbor; but again, significant increases in flooding also occur for the other tested tide phases. As a further illustration of CRT results, Figure 21 shows time series of surface elevations computed at Battery Point (Station #9 in Fig. 7), for the 4 tide phases of dynamic simulations, compared to results computed over a static water level corresponding to the local high tide (which is slightly higher, at +0.7 NAVD88, than the average +0.64 value). For the first three tide phases, maximum surface elevations in the dynamic simulations are higher, by 0.2-0.5 m, than for the static level. It is only for the 3 h delayed phase that maximum dynamic elevations are lower than in computations over the static level; this is because the tide elevation becomes too low, even negative, in this case (for reference, tide elevations are plotted in the figure for each tide phase).

Maximum envelopes of surface elevations computed for each of the three incident tsunamis, over the 4 tested tide phases (i.e., envelopes of the dynamic simulations on which the difference plots of Figs. 16, 17 and 18 are based, plus the 3 h delay case), are potted in Figure 19; and their difference with the envelope of the same results over a static tide level (Fig. 14) is plotted in Fig. 20. These results confirm that nearly everywhere in the HRE, inside/outside NY harbor, along southern Manhattan and across in Hoboken, NJ, and in the East River, the maximum coastal flooding is larger when computed in a dynamic tide-tsunami simulation than over a static level, by up to 0.8 m. This is less so for the PRT tsunami, which is made of longer and smaller amplitude waves and more particularly so for the CVV and CRT tsunamis, which are made of shorter and larger waves. For these cases, the figures show that, for instance, in southern Manhattan, Hoboken and the East River, dynamic tide-tsunami interaction effects add 0.6 to 0.8 m of flooding on top of a 1.8 to 2 m elevation computed over the static level (i.e., about a 30% increase), and a little more locally; so this quite significant. For the CRT case, outside NY harbor, 0.6 to 0.8

m are added on top of a 2.8 m coastal flooding (i.e., about a 25-30% increase).

A more detailed analysis of time series of surface elevations and currents is presented in the next section, to better understand the physical mechanisms of tide-tsunami interactions that lead to increased coastal flooding.

6 Detailed analysis of results

To better understand the physical processes that govern tide-tsunami interactions in the simulations presented above, in the following, we perform a more detailed analysis of time series of results obtained in grid G1, at 5 numerical gages/stations located in the HRE from the entrance to Rarity Bay to the upper part of the Hudson River (see station locations in Fig. 22). These results are shown in Figures 23 to 28, for the currents and surface elevations computed for the 3 PMTs and the tide, and for the three main phases of the tide considered here, i.e.,1.5 h before, concurrent with, and 1.5 h after high tide.

More specifically, Figures 23, 24, and 25 show, for the three PMTs, respectively, and for the 3 considered phases of the tide, time series of currents for the tide and tsunami (over a static MHW) alone, as well as for the linear and dynamic (nonlinear) superposition of these; all currents are projected on the local direction of tsunami propagation. Then, Figures 26, 27, and 28 show, for the same cases, time series of surface elevations and (projected) currents for the tide and surface elevations for the tsunami (over a static MHW) alone, as well as for the dynamic (nonlinear) superposition of tide and tsunami; the tide current is provided in these plots to indicate whether it is a flooding (positive current) or an ebbing (negative current) tide. Note, to make for an easier comparison, surface elevation time series for the tsunami simulations (static or dynamic) have been detided by subtracting the corresponding tide surface elevations (i.e., static MHW level or dynamic level). In all the time series, it is observed that higher frequency oscillations that are present at Station # 1 in each PMT wave train gradually disappear as the tsunamis propagate up the HRE, whether over a static or dynamic level, as a result of the increased dissipation by bottom friction in shallow water.

Regarding currents, while there are significant differences between tide phases, stations, and tsunamis, we see that in all cases there is a marked and often large difference between the linear and nonlinear

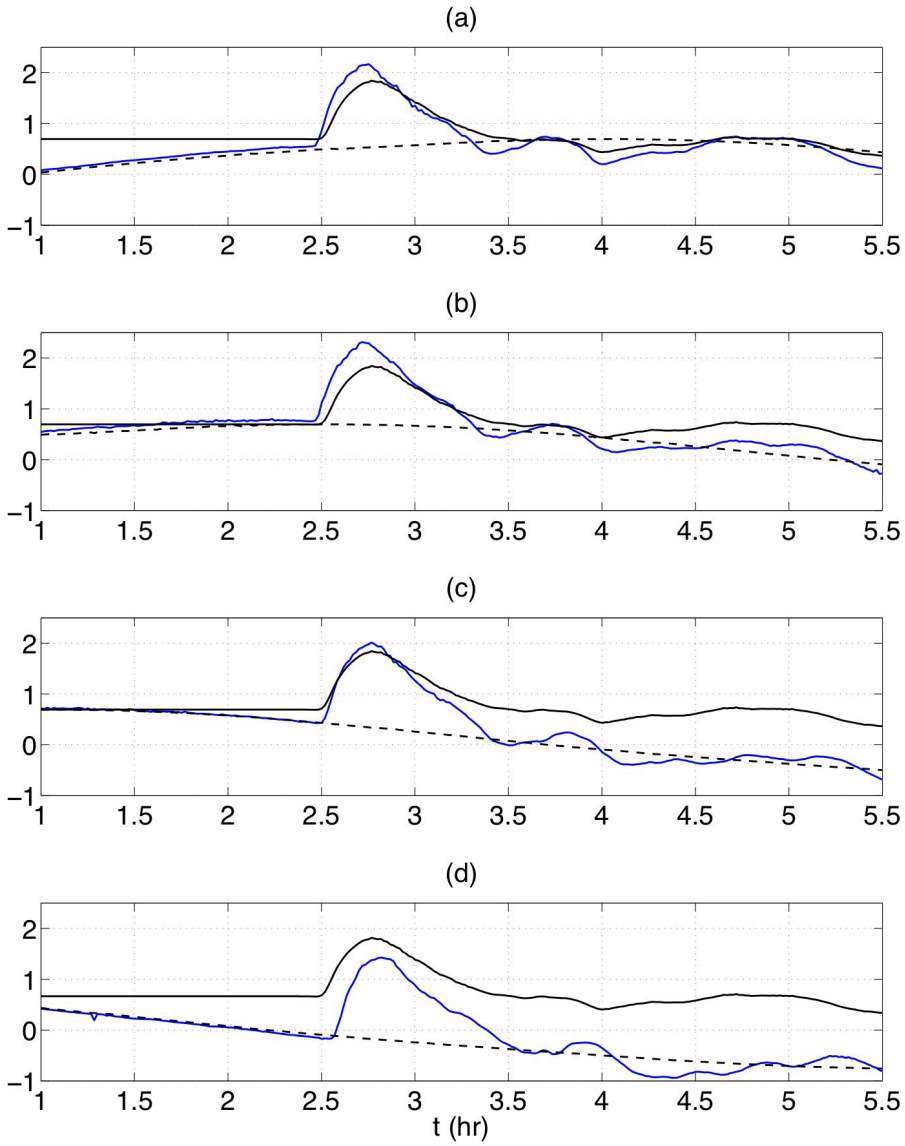

Figure 21: Time series of surface elevations (meters referenced to NAVD88) computed at Battery Point (Station #9 in Fig. 7) for the CRT SMF proxy tsunami: (blue lines) dynamic tide-tsunami simulations; (black lines) tsunami simulations over a static level equal to the local maximum tide (tide elevations are shown as dashed lines for reference). Dynamic simulations were performed for the leading tsunami crest arriving at Sandy Hook station at four phases of the tide (see Fig. 15) : (a) 1.5 h before, (b) concurrent with, (c) 1.5 h after, and (d) 3 h after high tide.

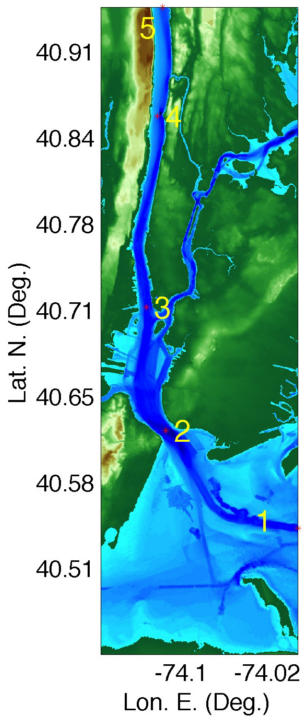

Figure 22: Locations of numerical gages/stations #1 to 5 in the HRE, where time series of surface elevations and currents are computed in grid G1, to perform a more detailed analysis of tide-tsunami interactions. See Figures 23 to 28 for results.

combinations of tide and tsunami currents. While at Station #1, near the entrance to Raritan Bay, the linear superposition of currents often has a larger maximum than the nonlinear combination, it is the opposite for stations #2 to #5, further up the HRE, with the nonlinearly combined currents achieving larger (sometimes significantly) magnitudes than the linearly combined currents. Regarding elevations, the patterns in each figure are similarly divided between the same stations. At Station #1, as would be expected from elementary long wave theory, tsunami waves facing an opposite (ebbing) current increase in elevation and they decrease when traveling with the current, both as compared to the simulations performed over a static MHW level. At Stations #2 to #5, however, in all cases (i.e., of tsunamis and tide phase), the maximum surface elevations in the dynamically combined simulations are larger than for the static simulation, which is consistent with the systematically larger maximum currents and increased maximum inundation in the HRE mentioned before. While the precise physics governing this phenomenon remains unclear, it is likely that site specific effects play an important role; for instance, the sensitivity of wave refraction to phase speed in Raritan Bay could result in larger waves at the Narrows (Station #2, Figure 22).

It is thus confirmed, as could have been expected from wave theories, that the tide current, which is present in the dynamic tide-tsunami simulations, but absent in the static case, is primarily responsible for differences observed between the two sets of results. Tide currents exceed 1 m/s (2 kts) within grid G1, which is comparable to currents caused by the incoming PMTs. The similarity in current magnitude thus results in significant nonlinear interactions between the two long waves. At the entrance to Raritan Bay (Station #1 in Figure 22), slack tide occurs about 1 hour after high tide. In the Hudson River, the flooding current continues for more than two hours after high tide. Tsunami crests arriving 1.5 hours after high tide (during the first part of the ebb current), will experience a favorable current in the Hudson River because of this shift.

Differences between surface elevation time series for the dynamic tide-tsunami simulations and those for the tsunami propagating over a static MHW level thus result from nonlinear interactions between tide and tsunami currents. Additionally, results in Figs. 26 to 28 show that a favorable current during tidal flood causes a higher phase speed of the incident tsunamis and a slower one during ebb. In each case, during the flood, the (detided) dynamically combined tide-tsunami

elevation arrives before the elevation of the static simulation, and after the static case during the ebb; and this difference in arrival time progressively increases as the tsunamis propagate up the HRE (from Station #1 to 5).

7 Conclusions

The dynamic simulations of tide and tsunami interactions in the HRE have identified a systematic and significant increase in maximum surface elevation and inundation, as compared to simulations performed over a static MHW model, which are meaningful for tsunami hazard assessment. Figures 16, 17 and 18, which show maximum envelopes of differences between the dynamic and static results computed for the 3 main tide phases and for each PMT, and the envelopes of these in Fig. 20, indicate that areas with the largest increases in surface elevation are located near Staten Island and Coney Island outside of New York Harbor and in southern Manhattan and Hoboken inside the harbor.

In these areas, inundation maps developed based on static levels should be revised to include the additional flooding resulting from dynamic tide-tsunami interactions. As an example, differences in inundation obtained in the east coast of Staten Island are shown in Figure 29 for the static and dynamic simulations. These clearly indicate a significantly increased generation of tsunami flooding, particularly for the CVV and CRT SMF proxy tsunamis.

Overall, results also show that complex bathymetry and large tide currents are factors that can result in significant increase in surface elevation and inundation as compared to a static simulation. Hence, dynamic tide-tsunami effects are highly site specific and thus detailed, high-resolution, simulations must be performed to accurately computed them.

References

Abadie S., Harris J.C., Grilli S.T. and R. Fabre. Numerical modeling of tsunami waves generated by the flank collapse of the Cumbre Vieja Volcano (La Palma, Canary Islands): tsunami source and near field effects. *J. Geophys. Res.*, 117:C05030, doi:10.1029/2011JC007646, 2012.

Barkan, R., ten Brick, U.S., and J. Lin. Far field tsunami simulations of the 1755 Lisbon earthquake: Implication for tsunami hazard

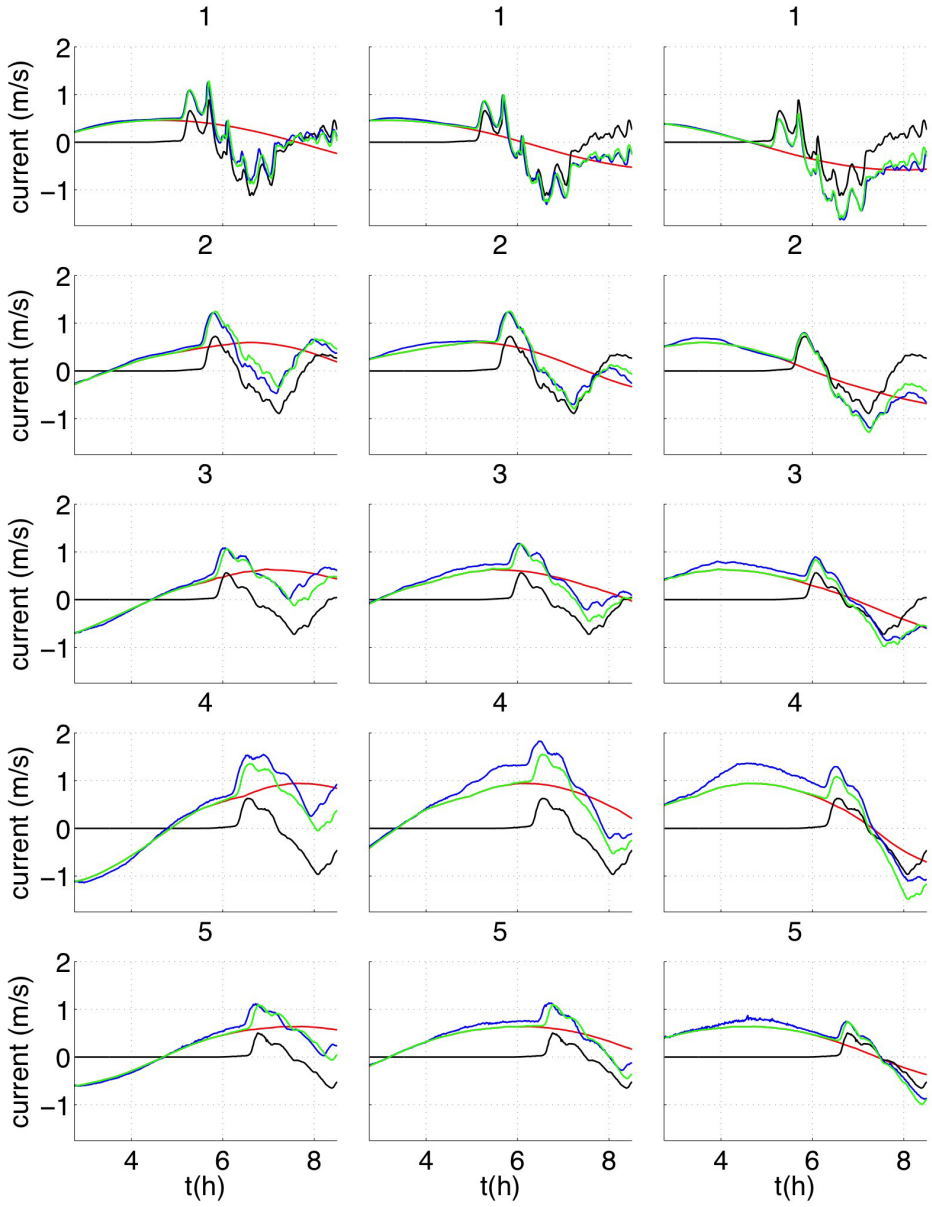

Figure 23: Time series of currents projected in the tsunami direction of propagation, at stations #1-5 (labels) in grid G1 (Fig. 22), for the PRT tsunami (black), tide (red), and their linear (green) and nonlinear (blue) combinations: 1.5 h before, concurrent with, and 1.5 h after high tide (left, middle, and right columns). Time is measured from the beginning of the event.

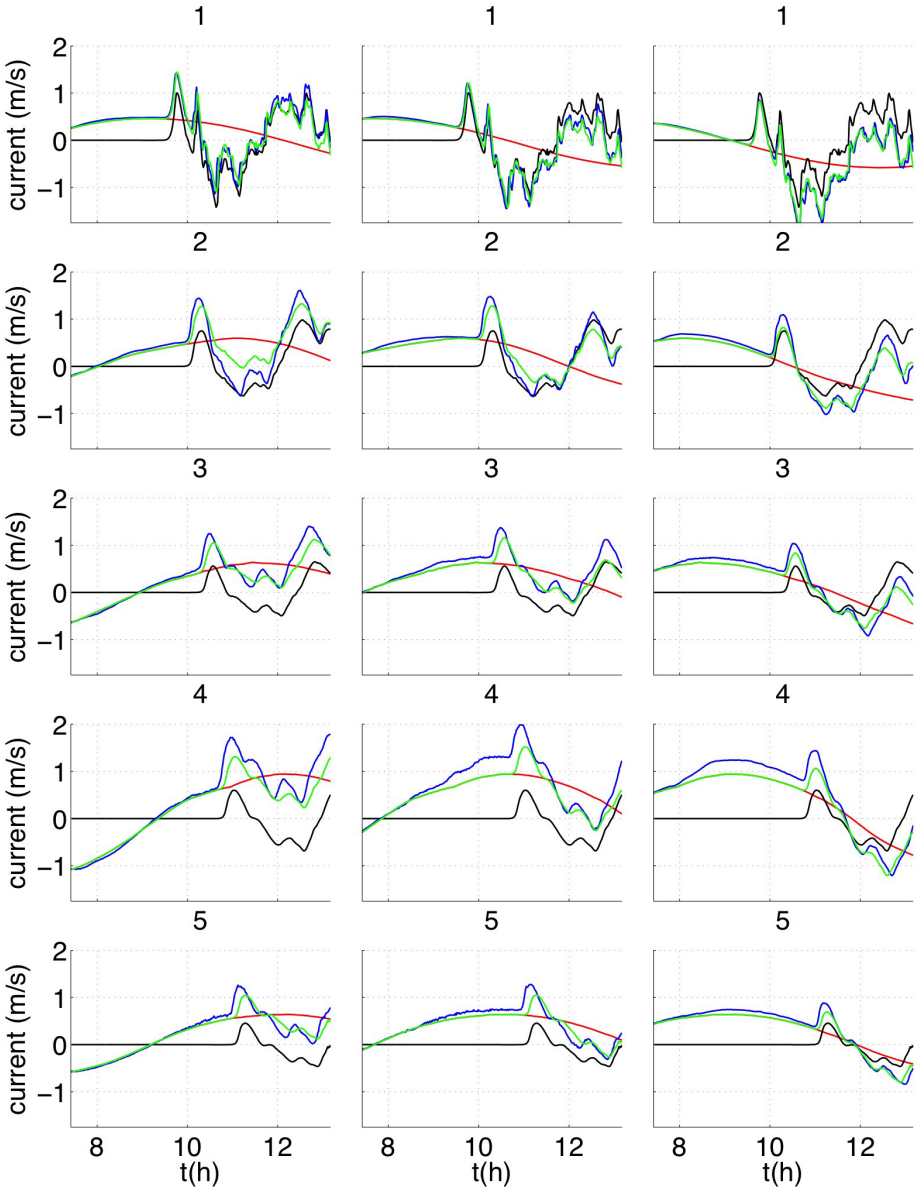

Figure 24: Same results as in Fig. 23 for the CVV tsunami.

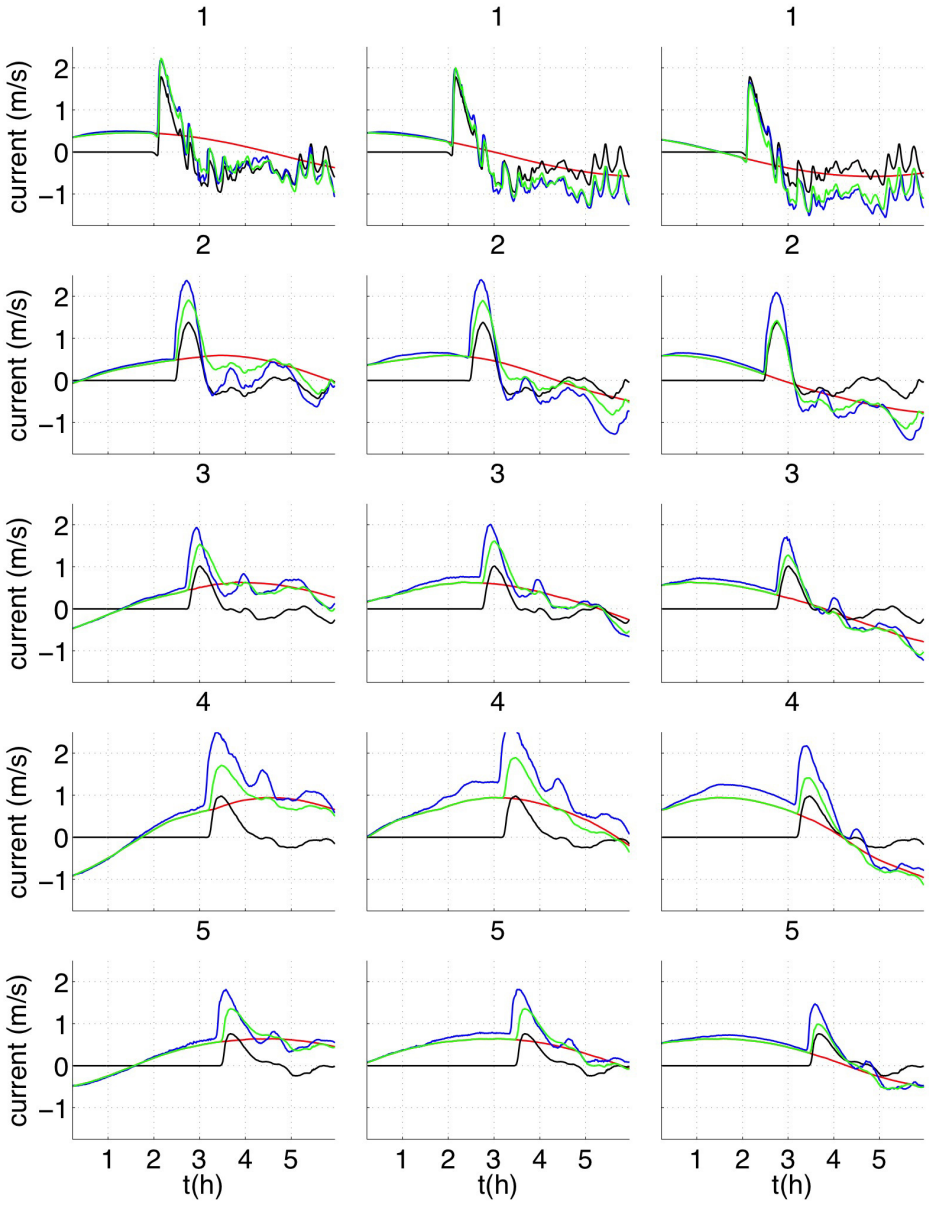

Figure 25: Same results as in Fig. 23 for the CRT SMF proxy tsunami.

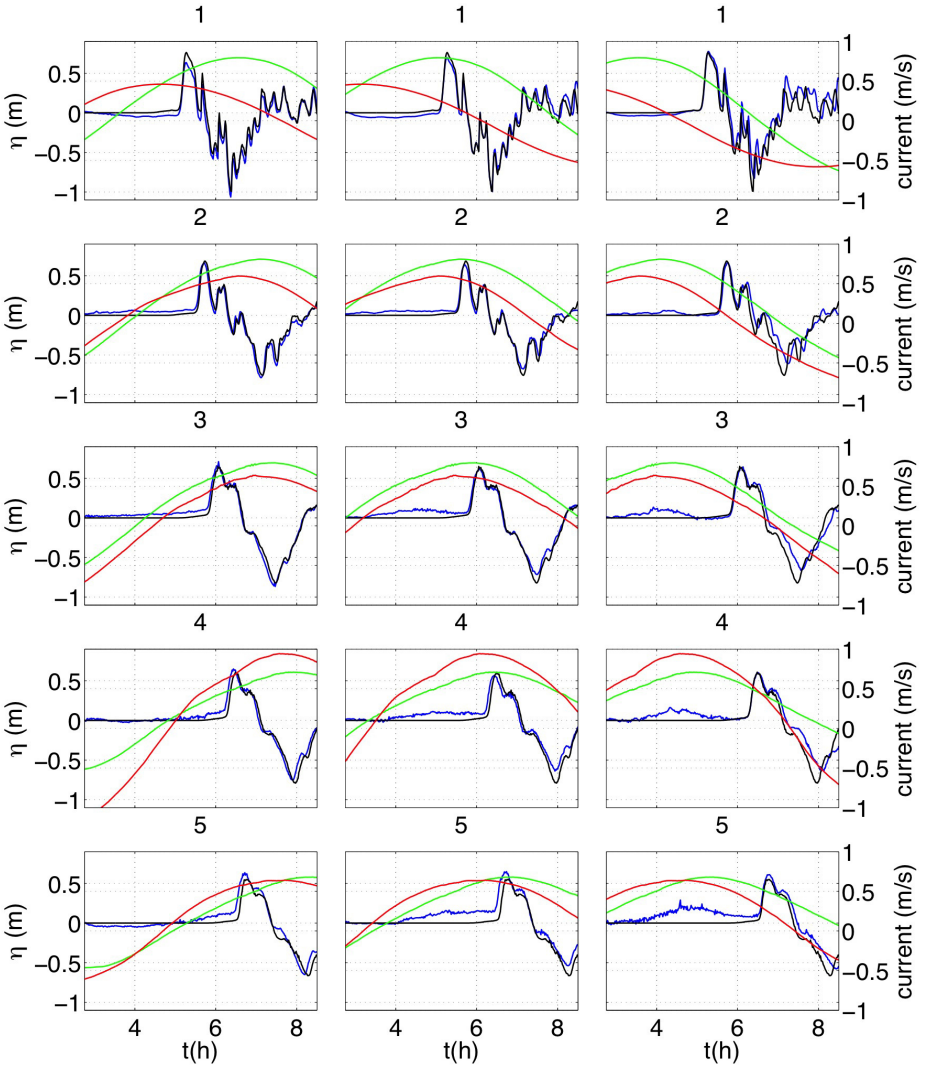

Figure 26: Time series at stations #1-5 (labels) in grid G1 (Fig. 22) of tidal currents projected in the tsunami direction of propagation (red), and surface elevations for the tide (green) and PRT tsunami: over static MHW level, relative to MHW level (black), and in dynamic combination with the tide (blue): 1.5 h before, concurrent with, and 1.5 h after high tide (left, middle, and right columns). Tsunami surface elevations (static or dynamic) have been detided by subtracting the corresponding tide surface elevations (i.e., static MHW level or dynamic level). Time is measured from the beginning of the event.

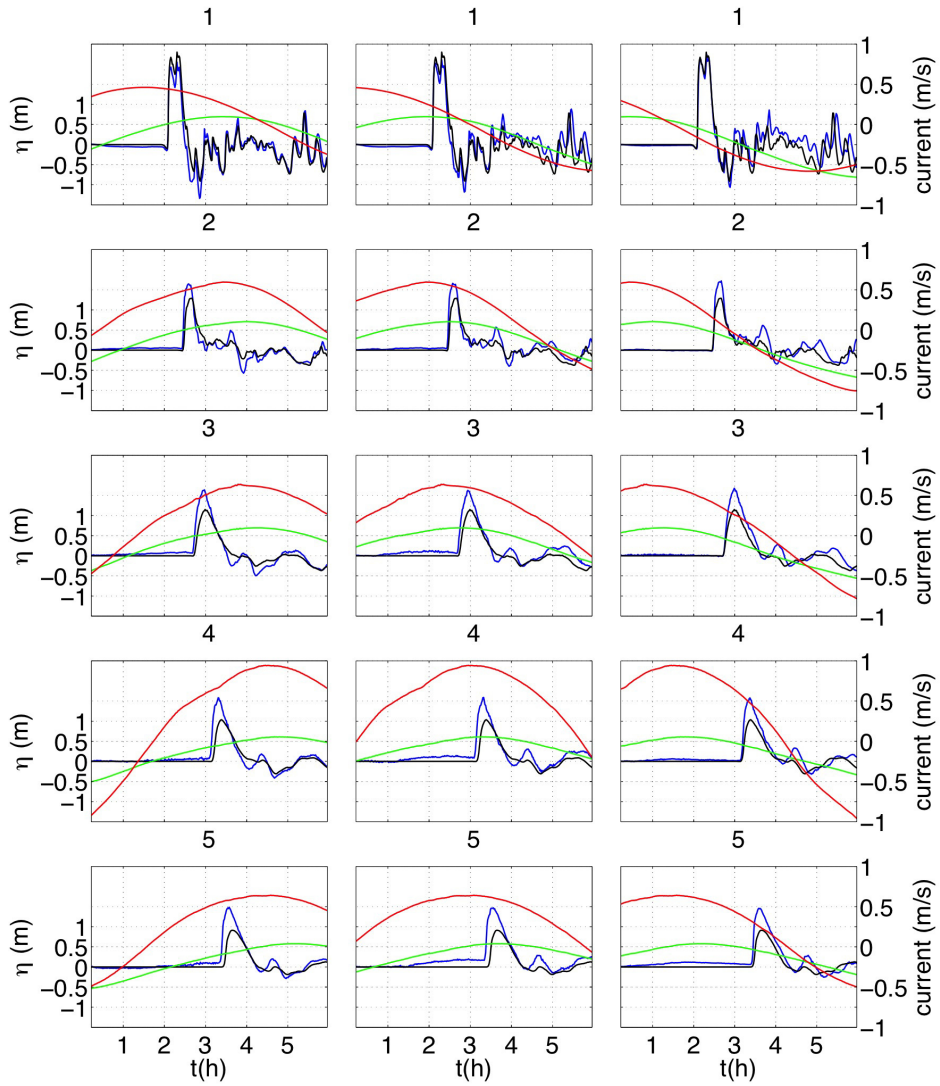

Figure 27: Same results as in Fig. 26 for the CVV tsunami.

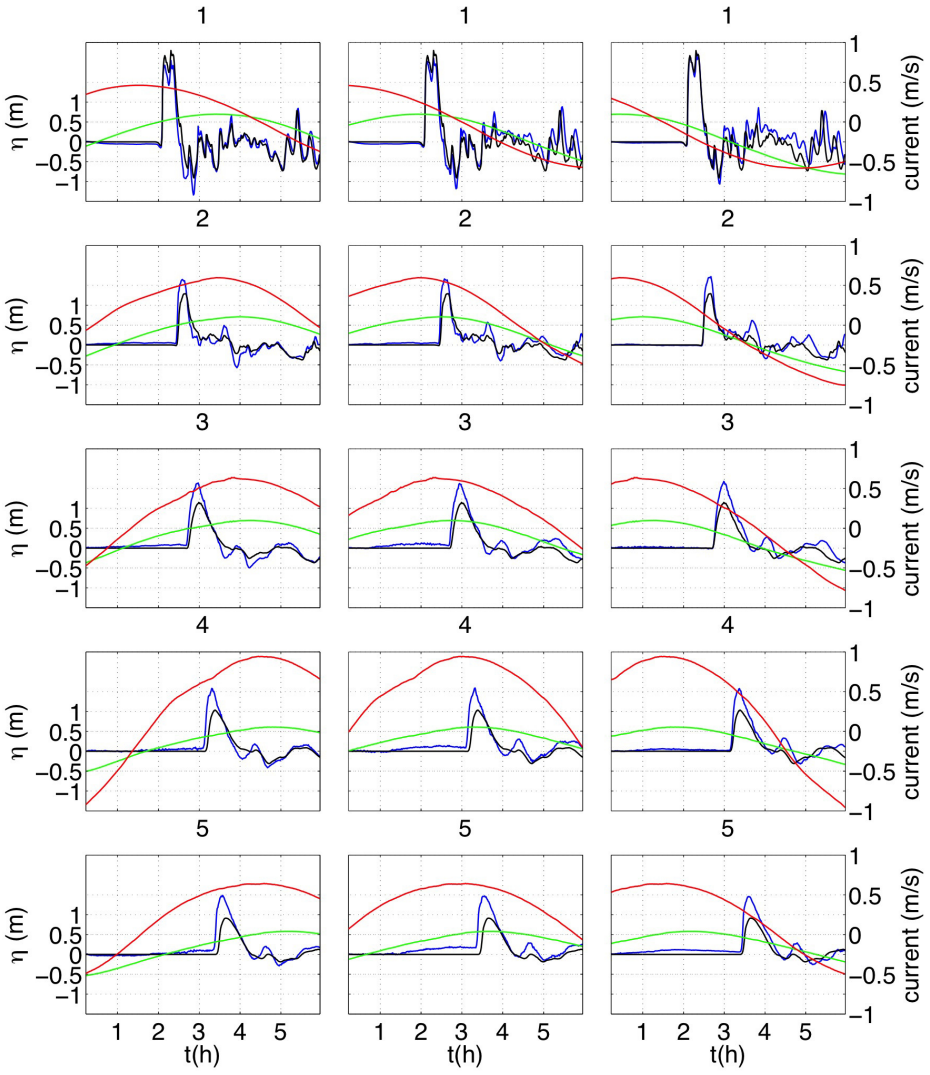

Figure 28: Same results as in Fig. 26 for the CRT SMF proxy tsunami.

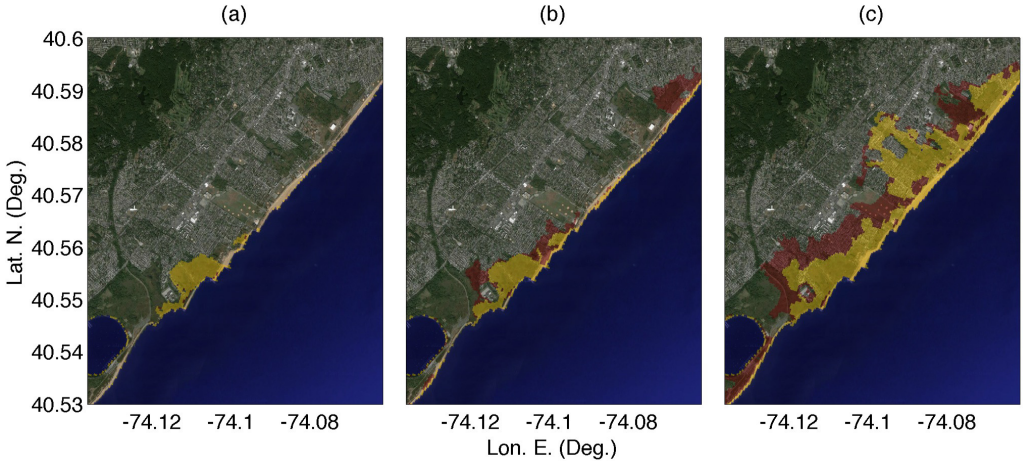

Figure 29: Comparison of tsunami inundation areas in eastern Staten Island from : (red) maximum envelopes computed over 4 tidal phases in dynamic tide-tsunami simulations (Fig. 19); and (yellow) the linear superposition of tsunamis over a static tide level (local MHW), for the three considered PMTs: (a) PR, (b) CVV, and (c) CRT SMF proxy.

to the U.S. East Coast and the Caribbean. *Marine Geology*, 264:109-122, 2009.

Dean, R.G., and R.A. Dalrymple. *Water wave mechanics for engineers and scientists*. World Scientific, Advanced Series on Ocean Engineering, Prentice-Hall, 1991.

Egbert G.D., Bennett A.F., and M.G.G. Foreman. TOPEX/POSEIDON tides estimated using a global inverse model. *J. Geophys. Res.*, 99(C12):24,821-24,852, 1994.

Federal Emergency Management Agency (FEMA). Region II Storm Surge Project - Coastal Terrain Processing Methodology. Department of Homeland Security, 500 C Street, SW Washington DC, 20472, 2014.

Geist E., P. Lynett, and J. Chaytor. Hydrodynamic modeling of tsunamis from the Currituck landslide. *Marine Geology*, 264:41-52, 2009.

Gica, E., M. C. Spillane, V. V. Titov, C. D. Chamberlin, and J. Newman. Development of the forecast propagation database for

NOAAs Short-Term Inundation Forecast for Tsunamis. NOAA Tech. Memo. OAR PMEL-139, 2008.

Grilli S.T., Dubosq S., Pophet N., Pérignon Y., Kirby J.T., and F. Shi. Numerical simulation and first-order hazard analysis of large co-seismic tsunamis generated in the Puerto Rico trench: near-field impact on the North shore of Puerto Rico and far-field impact on the US East Coast. *Natural Hazards and Earth System Sciences*, dpi:10:2109-2125, 2010.

Grilli A.R. and S.T. Grilli. Modeling of tsunami generation, propagation and regional impact along the U.S. East Coast from the Azores Convergence Zone. Research Report no. CACR-13-04, 20 pps., http://personal.egr.uri.edu/grilli//grilli-grilli-cacr-13-04, 2013a.

Grilli A.R. and S.T. Grilli. Modeling of tsunami generation, propagation and regional impact along the upper U.S East coast from the Puerto Rico trench. Research Report no. CACR-13-02, 18 pps., http://personal.egr.uri.edu/grilli//grilli-grilli-cacr-13-02, 2013b.

Grilli S.T., Ioualalen M., Asavanant J., Shi F., Kirby J.T., and P. Watts. Source constraints and model simulation of the December 26, 2004 Indian Ocean tsunami. Journal of Waterway, Port, Coastal, and Ocean Engineering, 33:414-428, 2007.

Grilli, S.T., J.C. Harris, T. Tajalli-Bakhsh, T.L. Masterlark, C. Kyriakopoulos, J.T. Kirby and F. Shi. Numerical simulation of the 2011 Tohoku tsunami based on a new transient FEM co-seismic source: Comparison to far- and near-field observations. *Pure and Applied Geophysics*, 170:1333-1359, doi:10.1007/s00024-012-0528-y, 2013.

Grilli S.T., O'Reilly C., Harris J.C., Tajalli-Bakhsh T., Tehranirad B., Banihashemi S., Kirby J.T., Baxter C.D.P., Eggeling T., Ma G. and F. Shi. Modeling of SMF tsunami hazard along the upper US East Coast: Detailed impact around Ocean City, MD. Natural Hazards, 76(2):705-746, doi: 10.1007/s11069-014-1522-8, 2015.

Grilli, S.T., Taylor, O.-D. S., Baxter, D.P. and S. Maretzki. Probabilistic approach for determining submarine landslide tsunami hazard along the upper East Coast of the United States. *Marine Geology*, 264(1-2):74-97, doi:10.1016/j.margeo.2009.02.010, 2009.

Ioualalen M., Asavanant J., Kaewbanjak N., Grilli S.T., Kirby J.T. and P. Watts, Modeling the 26th December 2004 Indian Ocean tsunami: Case study of impact in Thailand. Journal of Geophysical Research, 112:C07024, doi:10.1029/2006JC003850, 2007.

Kirby J.T., Shi F., Tehranirad B., Harris J.C. and S.T. Grilli. Dispersive tsunami waves in the ocean: Model equations and sensitivity to dispersion and Coriolis effects. *Ocean Modeling*, 62:39-55, doi:10.1016/j.ocemod.2012.11.009, 2013.

Kowalik, Z. and A. Proshutinsky. Tsunami-tide interactions: A cook inlet case study. *Continental Shelf Research*, 30(6):633642, 2010.

Kowalik, Z., Proshutinsky, T., and A. Proshutinsky. Tide-tsunami interactions. *Science of Tsunami Hazards*, 24(4):242256, 2006.

Ma G., Shi F. and J.T. Kirby. Shock-capturing non-hydrostatic model for fully dispersive surface wave processes. Ocean Modell., 43-44:22-35, 2012.

NOAA-NGDC. National Geophysical Data Center, U.S. Coastal Relief Model, Retrieved December 2013, http://www.ngdc.noaa.gov/mgg/coastal/crm.html, 2013.

Okada, Y. Surface deformation due to shear and tensile faults in a half space. *Bull. Seismol. Soc. America*, 75(4):1135-1154, 1985.

Shi F., Kirby J.T., Harris J.C., Geiman J.D., and S.T. Grilli. A high-order adaptive time-stepping TVD solver for Boussinesq modeling of breaking waves and coastal inundation. *Ocean Modelling*, 43-44:36-51, 2012a.

Shi, F., Kirby, J. T. and B. Tehranirad. Tsunami benchmark results for spherical coordinate version of FUNWAVE-TVD (Version 1.1). Research Report No. CACR-12-02, Center for Applied Coastal Research, Univ. of Delaware, Newark, 2012b.

Stammer, D., Ray, R. D., Andersen, O. B., Arbic, B. K., Bosch, W., Carrere, L., Cheng, Y., Chinn, D. S., Dushaw, B. D., Egbert, G. D., Erofeeva, S. Y., Fok, H. S., Green, J. A. M., Griffiths, S., King, M. A., Lapin, V., Lemoine, F. G., Luthcke, S. B., Lyard, F., Morison, J., Muller, M., Padman, L., Richman, J. G., Shriver, J. F., Shum, C. K., Taguchi, E., and T. Yi. Accuracy assessment of global barotropic ocean tide models. *Reviews of Geophysics*, 52(3):243282, 2014.

US Geological Survey. Estimates of monthly and annual net discharge, in cubic feet per second, of Hudson River at New York, N.Y. (mouth). *U.S. Department of the Interior*, http://ny.water.usgs.gov/projects/dialerplots/HudsonRatNYCFreshwaterDischarge.htm, 2010.

Tajali-Bakhsh, T.S., Grilli, S.T., and A.R. Grilli. Dynamic tide effects on tsunami coastal hazard in large estuaries: Case of the chesapeake bay/James River, USA. Department of Ocean Engineering, University of Rhode Island, 42 pgs, 2014.

Tehranirad B., Shi F., Kirby, J.T., Harris J.C. and S.T. Grilli. Tsunami benchmark results for fully nonlinear Boussinesq wave model FUNWAVE-TVD, Version 1.0. Technical report, No. CACR-11-02, Center for Applied Coastal Research, University of Delaware, 2011.

Tehranirad, B., Banihashemi, S., Kirby, J. T., Callahan, J. A. and F. Shi. Tsunami inundation mapping for Ocean City, MD NGDC DEM. *Research Report No. CACR-14-04*, Center for Applied Coastal Research, Department of Civil and Environmental Engineering, University of Delaware, 2014.

Tehranirad B., Harris J.C., Grilli A.R., Grilli S.T., Abadie S., Kirby J.T. and F. Shi. Far-field tsunami hazard in the north Atlantic basin from large scale flank collapses of the Cumbre Vieja volcano, La Palma. Pure Appl. Geophys., 28 pps., doi:10.1007/s00024-015-1135-5 (published online 7/21/15), 2015.

ten Brink, U., Twichell D., Geist E., Chaytor J., Locat J., Lee H., Buczkowski B., Barkan R., Solow A., Andrews B., Parsons T., Lynett P., Lin J., and M. Sansoucy. Evaluation of tsunami sources with the potential to impact the U.S. Atlantic and Gulf coasts. USGS Administrative report to the U.S. Nuclear Regulatory Commission, 300 pp., 2008.

ten Brink U.S., Chaytor J.D., Geist E.L., Brothers D.S. and B.D. Andrews. Assessment of tsunami hazard to the U.S. Atlantic margin. *Marine Geology*, 353:31-54, 2014.

Tolkova, E. Tide-tsunami interaction in Columbia River, as implied by historical data and numerical simulations. *Pure and Applied Geophysics*, 170(6-8):11151126, 2013.

Tolkova, E., Tanaka, H., and M. Roh. Tsunami observations in rivers from a perspective of tsunami interaction with tide and riverine flow. *Pure and Applied Geophysics*, 172(3-4):953968, 2015.

Ward S. N. and S. Day. Cumbre Vieja Volcano potential collapse at La Palma, Canary Islands. *Geophysical Research Letter*, 28:397-400, 2001.

Wei G., Kirby J.T., Grilli S.T. and R. Subramanya. A fully nonlinear Boussinesq model for free surface waves. Part I: Highly nonlinear unsteady waves. Journal of Fluid Mechanics, 294:71-92, 1995.

Yeh H., Tolkova E., Jay D., Talke S. and H. Fritz. Tsunami Hydrodynamics in the Columbia River. *J. Disaster Res.*, 7(5), 604-608, 2012.

Zhang, Y. L. J., Witter, R. C., and G. R. Priest. Tsunami-tide interaction in 1964 Prince Williams Sound tsunami. *Ocean Modelling*, 40(3-4):246259, 2011.